



The Ups and Downs of Accreting X-Ray Pulsars: Decade-long Observations with the Fermi Gamma-Ray Burst Monitor

C. Malacaria^{1,2,5} , P. Jenke³, O. J. Roberts², C. A. Wilson-Hodge⁴ , W. H. Cleveland², and B. Mailyan³
on behalf of the GBM Accreting Pulsars Program Team

¹ NASA Marshall Space Flight Center, NSSTC, 320 Sparkman Drive, Huntsville, AL 35805, USA

² Universities Space Research Association, Science and Technology Institute, 320 Sparkman Drive, Huntsville, AL 35805, USA

³ University of Alabama in Huntsville, NSSTC, 320 Sparkman Drive, Huntsville, AL 35805, USA

⁴ NASA Marshall Space Flight Center, Huntsville, AL 35812, USA

Received 2019 December 16; revised 2020 March 29; accepted 2020 March 30; published 2020 June 16

Abstract

We review more than 10 yr of continuous monitoring of accreting X-ray pulsars with the all-sky Gamma-ray Burst Monitor (GBM) aboard the Fermi Gamma-ray Space Telescope. Our work includes data from the start of GBM operations in 2008 August, through to 2019 November. Pulsations from 39 accreting pulsars are observed over an energy range of 10–50 keV by GBM. The GBM Accreting Pulsars Program performs data reduction and analysis for each accreting pulsar and makes histories of the pulse frequency and pulsed flux publicly available. We examine in detail the spin histories, outbursts, and torque behaviors of the persistent and transient X-ray pulsars observed by GBM. The spin period evolution of each source is analyzed in the context of disk-accretion and quasi-spherical settling accretion-driven torque models. Long-term pulse frequency histories are also analyzed over the GBM mission lifetime and compared to those available from the previous Burst and Transient Source Experiment all-sky monitoring mission, revealing previously unnoticed episodes in some of the analyzed sources (such as a torque reversal in 2S 1845–024). We obtain new, or update known, orbital solutions for three sources. Our results demonstrate the capabilities of GBM as an excellent instrument for monitoring accreting X-ray pulsars and its important scientific contribution to this field.

Unified Astronomy Thesaurus concepts: Neutron stars (1108); Accretion (14); Stellar accretion disks (1579); X-ray transient sources (1852)

1. Introduction

Accreting X-ray Pulsars (XRP) were discovered almost 50 yr ago, when X-ray pulsation was detected from Cen X-3 and Her X-1 (Giacconi et al. 1971; Tananbaum et al. 1972) and was subsequently interpreted as a rotating, magnetized Neutron Star (NS) accreting the stellar wind expelled by a donor companion star (Pringle & Rees 1972; Davidson & Ostriker 1973; Lamb et al. 1973). For magnetized NSs, where the magnetic field strength is $B \sim 10^{12}$ G, the stellar wind flow is disrupted by the magnetic pressure and channeled to the magnetic polar caps, the so-called “hotspots.” Here, the potential energy is converted into X-ray radiation with a luminosity L_{acc} of

$$L_{\text{acc}} \approx \frac{G M_{\text{NS}} \dot{m}}{R_{\text{NS}}} \quad (1)$$

where $M_{\text{NS}} = 1.4 M_{\odot}$ and $R_{\text{NS}} = 10$ km are the mass and radius, respectively, of a typical NS, and \dot{m} is the mass accretion rate.

The study of an XRP system consisting of a magnetized, accreting compact object and an optical companion is key to understanding the behavior of matter under extreme conditions and for probing the evolutionary paths of both the binary system and its individual components. The NS represents the final stage of the evolutionary track of massive stars as a supernova remnant, characterized by extreme densities, high magnetic and gravitational fields, and a very small moment of inertia. Therefore, knowledge is required from multiple

scientific disciplines in order to describe NSs in an astrophysical context (i.e., accretion processes, plasma physics, nuclear physics, electrodynamics, general relativity, and quantum theory). Furthermore, the presence of a donor companion makes these systems excellent laboratories for the study of additional astrophysical processes, such as the stellar wind environment, radiative effects, and matter transfer. Finally, the presence of an orbiting XRP makes these objects invaluable tools for the characterization of orbital elements and component masses.

The Milky Way and the Magellanic Clouds contain ~ 230 XRP. Recent reviews on XRP and their observational properties are given in Caballero & Wilms (2012), Walter & Ferrigno (2017), Maitra (2017), and Paul (2017). These systems have pulse periods that range from several ms to hours. For approximately half of those systems, their X-ray activity has only been observed serendipitously during transient episodes.

In this paper, we review more than 10 yr of observations of XRP with the Gamma-ray Burst Monitor (GBM), an all-sky, transient monitor aboard the Fermi observatory. The wide field of view and high timing capability of GBM are particularly suited to the continuous study of both transient and persistent XRP. As of 2019 November, GBM has detected a total of 39 XRP.

This paper is organized as follows. In Section 2, we briefly review the accretion physics onto magnetized compact objects. In Section 3, we describe the GBM instrument and its data handling. In Section 4, we describe the timing analysis applied

⁵ NASA Postdoctoral Fellow.

⁶ http://www.iasfbo.inaf.it/~mauro/pulsar_list.html

to the GBM raw data in order to obtain its data products. In Section 5, we give an overview of the binary systems observed by GBM and the type of X-ray activity that characterizes those systems. In Section 6, we describe each XRP system, providing a summary of their spin history as seen previously by other observatories and currently by GBM. Finally, in Section 7, we discuss the main results from the population study and from single systems in the most interesting cases. We summarize the importance of the GBM Pulsar Project in Section 8.

As the estimation of the spectral luminosity and measurement of the distance from the sources are important aspects of this work, we describe them separately in the Appendices A and B, respectively.

2. Accretion Physics onto Magnetized Neutron Stars

When accretion occurs onto a magnetized NS, the accreted material does not flow smoothly onto the surface of the compact object but is mediated by the NS’s magnetic field (Pringle & Rees 1972). At a certain distance from the NS surface, namely at the Alfvén radius r_A , the energy density of the magnetic field balances the kinetic energy density of the infalling material:

$$r_A = \left(\frac{\mu^4}{2GM\dot{M}} \right)^{1/7} = 6.8 \times 10^8 \dot{M}_{10}^{-2/7} \mu_{30}^{4/7} M_{1.4}^{-1/7} \text{ cm} \quad (2)$$

where \dot{M}_{10} is the accreted mass in units of $10^{-10} M_\odot \text{ yr}^{-1}$, μ_{30} is the magnetic moment in units of 10^{30} G cm^3 (corresponding to a typical magnetic field strength of 10^{12} G at the NS surface), and $M_{1.4}$ is the mass of the NS in units of $1.4 M_\odot$. The material can then penetrate the NS magnetic field via Rayleigh–Taylor and Kelvin–Helmholtz instabilities and when accretion is mediated through an accretion disk via magnetic field reconnection with small-scale fields in the disk and turbulent diffusion (Arons & Lea 1976; Ghosh & Lamb 1979a; Kulkarni & Romanova 2008, and references therein). In a disk, the magnetic threading produces a broad transition zone composed of two regions: a broad outer zone, where the disk angular velocity is nearly Keplerian, and a narrow inner zone or boundary layer, where the disk angular velocity significantly departs from the Keplerian value. The outer radius of the boundary layer is identified as the magnetospheric radius r_m :

$$r_m = k r_A \quad (3)$$

where the dimensionless parameter k , also called the coupling factor, is ~ 0.5 as given by Ghosh & Lamb (1979a), but it ranges from 0.3 to 1 in later models (Wang 1996; Li 1997; Li & Wang 1999; Long et al. 2005; Bessolaz et al. 2008; Zanni & Ferreira 2013; Dall’Osso et al. 2016, and references therein). It can be more generally considered as a function of the accretion rate, $k(\dot{M})$, and of the inclination angle between the neutron star rotation and magnetic field axes, and it can be significantly smaller than that obtained in the model by Ghosh & Lamb (1979a; see, e.g., Bozzo et al. 2009).

Disk-driven accretion can be inhibited by a centrifugal barrier if the pulsar magnetosphere rotates faster than the Keplerian velocity of the matter in the disk. This condition is realized when the inner disk radius, coincident with the magnetospheric radius r_m , is greater than the co-rotation radius, r_{co} , at which the Keplerian angular disk velocity ω_{co} is equal to

the angular velocity of the NS, $\sqrt{GM_{\text{NS}}/r_{\text{co}}}$:

$$r_{\text{co}} = \left(\frac{GM_{\text{NS}} P_s^2}{4\pi^2} \right)^{1/3} \quad (4)$$

where $\omega = 2\pi/P_s$ is the rotational frequency of the NS, and P_s is the NS spin. For a standard NS mass of $1.4 M_\odot$, the co-rotation radius is of the order of $r_{\text{co}} = 1.7 \times 10^8 P_s^{2/3} \text{ cm}$.

The relative positions of these radii determine the accretion regime at work, driven by the possible onset of (either a magnetic or centrifugal) barrier that inhibits direct wind accretion, also called the “gating” mechanism (Illarionov & Sunyaev 1975; Stella et al. 1985; Bozzo et al. 2008). Different regimes of plasma cooling also play a role in quasi-spherical wind-accretion onto slowly rotating NSs (Shakura et al. 2012, 2013; Shakura & Postnov 2017). In these systems, a hot shell forms above the NS magnetosphere and, depending on the mass accretion rate, can enter the magnetosphere either through inefficient radiative plasma cooling or by efficient Compton cooling. At the same time, the plasma mediates the angular momentum removal from the rotating magnetosphere by large-scale convective motions.

When $r_m > r_{\text{co}}$, the centrifugal barrier rises and mass is propelled away or halted at the boundary, rather than being accreted. This carries angular momentum from the NS, which consequently begins to spin down, and conditions become favorable for accretion via the propeller mechanism as the star enters this regime (Illarionov & Sunyaev 1975). However, for $r_m < r_{\text{co}}$, matter and thus angular momentum, is transferred to the spinning NS. Accordingly, in the case of disk accretion, the total torque N that the disk exerts on the NS is composed of two terms:

$$N = N_0 + N_{\text{mag}}, \quad (5)$$

where $N_0 = \dot{M} \sqrt{GM r_m}$ is the torque produced by the matter leaving the disk at r_m to accrete onto the NS, while $N_{\text{mag}} = -\int_{r_m}^{\infty} B_\phi B_z r^2 dr$ is the torque generated by the twisted magnetic field lines threading the disk outside r_m . Following Ghosh & Lamb (1979a, 1979b), the total torque in Equation (5) can also be expressed as

$$N = n(\omega_s) \dot{M} \sqrt{GM r_{\text{co}}}, \quad (6)$$

where n is a dimensionless torque that is a function of the fastness parameter ω_s ,

$$\omega_s = \frac{\nu_s}{\nu_k} = \left(\frac{r_{\text{in}}}{r_{\text{co}}} \right)^{3/2}, \quad (7)$$

where ν_s and ν_k are the spin frequency and the Keplerian frequency, respectively. Accretion from a disk leads to a spin period derivative (Ghosh et al. 1977; Ghosh & Lamb 1979a, 1979b) equal to

$$-\dot{P} = 5.0 \times 10^{-5} \mu_{30}^{2/7} n(\omega_s) R_{\text{NS}_6}^{6/7} M_{1.4}^{-3/7} I_{45}^{-1} P_s^2 L_{37}^{6/7} \text{ s s}^{-1}, \quad (8)$$

where R_{NS_6} is the NS radius in units of 10^6 cm , I_{45} is the NS moment of inertia in units of 10^{45} g cm^2 , and L_{37} is the bolometric luminosity in the X-ray band (1–200 keV) in units of $10^{37} \text{ erg s}^{-1}$.

For $0 < \omega_s < 0.9$, a good approximation of the dimensionless torque is (Klus et al. 2013):

$$n(\omega_s) = 1.4(1 - 2.86 \omega_s)(1 - \omega_s)^{-1}, \quad (9)$$

which, for $M_{\text{NS}} = 1.4 M_\odot$ and $R_{\text{NS}} = 10$ km, results in a torque (Ho et al. 2014) of

$$-\dot{P} = 7.1 \times 10^{-5} \text{ s yr}^{-1} k^{1/2} \times (1 - \omega_s) \mu_{30}^{2/7} (P L_{37}^{3/7})^2. \quad (10)$$

Equation (10) is widely used in the literature to study accretion disk related phenomena of spin derivatives observed in accretion XRPCs.

On the other hand, the quasi-spherical accretion model has been introduced to explain the behavior of wind-accreting systems that show long-term spin period evolution (González-Galán et al. 2012, 2018; Shakura et al. 2012; Postnov et al. 2015). This model describes two different accretion regimes, separated by a critical mass accretion rate $\dot{y} = \dot{M}/M_{\text{cr}}$, corresponding to a luminosity of $4 \times 10^{36} \text{ erg s}^{-1}$. At lower luminosities, an extended quasi-static shell is formed by the matter that is gravitationally captured by the NS and subsonically settled down onto the magnetosphere. The quasi-static shell mediates the exchange of angular momentum between the captured matter and the NS magnetosphere by turbulent viscosity and convective motions. Both spin-up and spin-down are possible in the subsonic regime, even if the specific angular momentum of the accreted matter is prograde. As the accretion rate increases above the critical value, the flow near the Alfvén surface becomes supersonic and a freefall gap appears above the magnetosphere due to the strong Compton cooling, causing the accretion to become highly unstable. In this regime, depending on the sign of the specific angular momentum, either spin-up or spin-down is possible.

The quasi-spherical accretion model also takes into account the coupling of the rotating matter with the magnetosphere at different regimes. A strong coupling regime is realized for rapidly rotating magnetospheres, in which the exchange of angular momentum between the accreted matter and the NS can be described as

$$I\dot{\omega} = K_{\text{mag}} + K_{\text{surf}} \quad (11)$$

where I is the NS's moment of inertia, K_{mag} is the contribution to the spin frequency evolution brought by the plasma-magnetosphere interactions at the Alfvén radius and can be either positive or negative, and K_{surf} is the spin-up contribution due to the angular momentum returned by the matter accreted onto the NS (see Equations (17)–(19) in Shakura et al. 2012). In the moderate coupling regime, a similar relation holds with different coupling coefficients (see Equations (27)–(29) in Shakura et al. 2012). To determine the main dimensionless parameters, the model was used to fit observations from a few long-period pulsars. Accordingly, the spin-down rate $\dot{\omega}_{\text{sd}}$ (where $\omega = 2\pi\nu$ is the angular frequency) observed in those systems is (Postnov et al. 2015)

$$\dot{\omega}_{\text{sd}} \approx 10^{-8} [\text{Hz day}^{-1}] \Pi_{\text{sd}} \mu_{30}^{13/11} \left(\frac{\dot{M}}{10^{16} \text{ g s}^{-1}} \right)^{3/11} \left(\frac{P_s}{100 \text{ s}} \right)^{-1} \quad (12)$$

where Π_{sd} is a parameter of the model, usually in the range 5–10, \dot{M} is the mass accretion rate normalized for a typical

luminosity of $10^{37} \text{ erg s}^{-1}$ (assuming $L = 0.1 \dot{M} c^2$), P_s is the pulsar spin period, and μ_{30} is the magnetic moment BR^3 in units of 10^{30} G cm^3 . The spin-up rate $\dot{\omega}_{\text{su}}$ is

$$\dot{\omega}_{\text{su}} \approx 10^{-9} [\text{Hz day}^{-1}] \Pi_{\text{su}} \mu_{30}^{1/11} \left(\frac{P_{\text{orb}}}{10 \text{ days}} \right)^{-1} \left(\frac{\dot{M}}{10^{16} \text{ g s}^{-1}} \right)^{7/11} \quad (13)$$

where P_{orb} is the binary orbital period, and $\Pi_{\text{su}} \approx \Pi_{\text{sd}}$ (Shakura et al. 2014).

3. The Fermi GBM X-Ray Monitor

GBM is an unfocused, background-dominated, all-sky instrument aboard the Fermi Gamma-ray Space Telescope (Meegan et al. 2009). It consists of 14 uncollimated, inorganic scintillator detectors: 12 thallium-doped sodium iodide (NaI) detectors and two bismuth germanate (BGO) detectors. The NaI detectors have an effective energy range of $\approx 8 \text{ keV}$ – 1 MeV , while the BGOs cover an energy range from $\approx 200 \text{ keV}$ – 40 MeV . As the emission of accreting pulsars is dominant only below $\sim 100 \text{ keV}$, data from the BGO detectors will not be used in this work. The NaI detectors are arranged into four clusters of three detectors, placed around each corner of the spacecraft in such a fashion that any source un-occulted by the Earth will illuminate at least one cluster.

GBM has three continuous (C) data types: CTIME data, with a nominal time resolution of 0.256 s and eight energy channels used for event detection and localization, CSPEC data, with a nominal time resolution of 4.096 s and 128 energy channels used for spectral modeling, and continuous time tagged event (CTTE) data with timestamps for individual photon events ($2 \mu\text{s}$ precision) over 128 energy channels. The latter has been available since 2012 November.

Even though GBM is devoted to hunting Gamma-ray Bursts, it has proven to be an excellent tool in the monitoring of other transient X-ray sources as well. Consequently, the GBM Accreting Pulsars Program⁷ (GAPP) was developed, with the aim of analyzing pulsars detected by GBM. In the context of the GAPP, two different pulse search strategies have been implemented: the daily blind search and the targeted (i.e., source-specific) search. The blind search consists of computing the daily fluxes for 26 directions (24 equally spaced on the Galactic plane, plus the Magellanic Clouds), using CTIME data type. For each direction, a blind Fast-Fourier Transform (FFT) search is performed between 1 mHz and 2 Hz (and up to 40 Hz with CTTE data). This ensures sensitivity to new sources, new outbursts from known sources, and pulsars whose pulse period is poorly constrained. Typically, only the first three GBM CTIME channels are used for this search: channels 0 (8 – 12 keV), 1 (12 – 25 keV), and 2 (25 – 50 keV). When a new source is detected through the blind search, its galactic longitude is interpolated from several directions, with the strongest signals in the power spectrum obtained by the FFT technique. The targeted search consists of an epoch-folding-based search over much smaller frequency ranges than the blind search method, which sometimes includes a search over the frequency derivative (see also Section 4). This is applied to known sources, which provides a higher sensitivity due to source-specific information such as the location, orbital parameters, and flux spectrum.

⁷ <https://gammaray.nsstc.nasa.gov/gbm/science/pulsars.html#>

For each source, GAPP extracts the pulsed portion of the pulsar’s signal (see Section 4). However, the un-pulsed flux of a discrete source can be obtained by fitting the steps in count rates that occur when the source rises or sets over the Earth’s horizon (see the GBM Earth Occultation Method—GEOM—web page⁸ and Wilson-Hodge et al. 2012).

The GAPP also inherited data from previous missions like the Burst and Transient Source Experiment (BATSE; Fishman et al. 1992; Bildsten et al. 1997) on board the Compton Gamma Ray Observatory (CGRO; Gehrels et al. 1994). One of the larger transient monitors in recent history, BATSE comprised eight NaI(Tl) large area detectors (LAD) each with 2025 cm² of geometric area (Fishman et al. 1992). A plastic charged particle anticoincidence detector was in front of each LAD, resulting in a lower energy threshold of ~ 20 keV. BATSE also included eight spectroscopy detectors that were not used for pulsar monitoring. The BATSE data consisted of nearly continuous time-binned data DISCLA (four channels, 1.024 s resolution) and CONT (16 channels, 2.048 s resolution). Generally, the first BATSE DISCLA channel, 20–50 keV, was used for pulsar monitoring. Comparatively, GBM detectors only have a Beryllium window in front and so they can reach ~ 8 keV, much lower than the BATSE LADs could. Despite the larger area of the BATSE detectors, the sensitivity is similar for GBM and BATSE for detecting outbursts of XRP, due to the added low-energy response of the GBM detectors along with the abundance of photons from the sources at those energies.

The pointing strategies for Fermi and CGRO differ, with Fermi operating in a sky-scanning mode and CGRO operating using inertial pointing. This resulted in the need to incorporate the detector response in an earlier step in the data analysis process for GBM to account for changing angular response as the spacecraft scanned the sky. Both missions were in low-Earth orbit, at a similar inclination and altitude, resulting in similar energy-dependent background rates. Both missions used the data when a source was visible above the Earth’s horizon for XRP analysis, resulting in similar exposure times of ~ 40 ks per day per source (depending on the source decl.).

The GAPP (see Section 4) is based on the technique developed for BATSE (Finger et al. 1999; Wilson-Hodge 1999; Wilson et al. 2002, 2003), which measured pulsed frequencies and pulsed flux for a number of XRP. Similarly to GBM, BATSE measured the un-pulsed flux for these sources using Earth occultation (Harmon et al. 2004).

We have now consolidated available BATSE data within the GAPP web pages⁹ so as to provide the community with 20 yr of pulsar monitoring spanning the last 30 yr. We show that the combination of BATSE and GBM data, spanning over almost three decades, allows for the long-term study of XRP that unveil otherwise unobservable phenomena.

4. Timing

4.1. Time Corrections

Before delving into the timing analysis of each detected pulsar, the epoch of observed events need to be corrected. All recorded epoch times, t , are barycentered to remove the effects of the satellite and the Earth’s revolutions, thus correcting the times as if the reference system is located at the center of mass

of the solar system. This correction process returns a final epoch time, t' , that takes into account the following contributions: the reference time t_0 , clock corrections Δ_{clock} (which account for differences between the observatory clocks and terrestrial time standards), the Roemer delay Δ_R (which accounts for the classical light travel time across the Earth’s orbit), the Einstein delay Δ_E (which accounts for the time dilation from the moving pulsar, observatory, and the gravitational redshift caused by the Sun and planets or the binary companion), and the Shapiro delay Δ_S (which represents the extra time required by the pulses to travel through the curved spacetime containing the solar system masses). Combining these terms in the equation for the final epoch, we have

$$t' = t - t_0 + \Delta_{\text{clock}} + \Delta_R + \Delta_E + \Delta_S.$$

If the orbit of the pulsar is known, a further correction is applied to the pulse arrival times, a correction known as orbital demodulation. The pulsar emission time, t^{em} , is computed from the Dynamical Barycentric Time (TDB) t' , as $t^{\text{em}} = \text{TDB} - z$, where z is the line-of-sight delay associated with the binary orbit of the pulsar (Deeter et al. 1981; Hilditch 2001):

$$z = a_x \sin i [\sin \omega (\cos E - e) + \sqrt{1 - e^2} \cos \omega \sin E]. \quad (14)$$

Here, a_x is the projected semimajor axis of the binary orbit, i is the orbit’s inclination relative to the plane of the sky, w is the periastron angle, and e is the binary orbit eccentricity, while E is the eccentric anomaly as expressed in Kepler’s equation

$$E - e \sin E = \frac{2\pi}{P_{\text{orb}}} (t^{\text{em}} - \tau_p), \quad (15)$$

where P_{orb} is the orbital period and τ_p is the periastron passage epoch.

4.2. The Phase Model

Pulsars represent excellent timing tools thanks to their very small moment of inertia, which allows precise measurements of the pulsar spin period and spin derivative via a pulsar timing technique. This involves the regular monitoring of the rotation of the NS, by tracking the arrival times of individual observed pulses. For this, an average pulse profile is produced at any time to be used as a template, along with the assumption that any given observed profile is a phase-shifted and scaled version of the template. This is encoded in the evolution of the pulse phase as a function of time ($\phi(t)$). This *pulse phase model* can be represented as a Taylor expansion around the reference time t_0 as

$$\phi(t) = \phi_0 + \nu_0(t - t_0) + \frac{1}{2}\dot{\nu}(t - t_0)^2 + \dots \quad (16)$$

where $\nu_0 = \nu(t = t_0)$ (and $\phi_0 = \phi(t = t_0)$), while $\dot{\nu}$ is the pulse frequency derivative. Pulsar timing deals with the determination of the pulse phase as accurately as possible in order to unambiguously establish the exact number of pulsar rotations between observations.

By fitting Equation (16) to the frequencies determined by the means of the power spectra or epoch-folding method, a preliminary phase model is estimated. This allows us to produce pulse profiles and, at the same time, to reduce the amount of data and computing time. In turn, pulse profiles are

⁸ https://gammaray.nsstc.nasa.gov/gbm/science/earth_occ.html

⁹ <https://gammaray.nsstc.nasa.gov/gbm/science/pulsars.html>

used to refine the phase model to a higher precision (i.e., by phase-connection, see Sections 4.3 and 4.4). To extract the periodic signal, two main methods are considered in this work: (1) the harmonic expansion, and (2) the search in frequency and frequency derivative.

4.3. Pulse Profiles Using a Harmonic Expansion

The pulsar periodic signal can be represented by a Fourier harmonic series:

$$m_k = \sum_{h=1}^N a_h \cos \{2\pi h \phi(t_k)\} + b_h \sin \{2\pi h \phi(t_k)\}, \quad (17)$$

where m_k is the model count rate at time t_k , a_h and b_h are the Fourier coefficients, h is the harmonic number, N is the number of harmonics, and $\phi(t_k)$ is the phase model. Similar to BATSE (Bildsten et al. 1997; Finger et al. 1999), six harmonics are typically used to represent the pulse profile. This results in a reasonable representation of all observed sources' pulse profiles, while the employment of additional harmonics does not improve the pulse structure significantly. To obtain the harmonic coefficients a_h and b_h , a fit is performed to minimize the χ^2 function:

$$\chi^2 = \sum_{k=1}^M \frac{\{x_k - (m_k + B_k)\}^2}{\sigma_{x_k}^2}, \quad (18)$$

where x_k and σ_k are the measured count rates and errors, respectively, $M = 2N$ is the number of statistically independent points, and B_k is the background (the unpulsed count rate level). For this technique to work, a careful choice of the data length has to be considered. The interval needs to be short enough to guarantee that the phase model is not significantly changed between the beginning and the end of the observation, while at the same time, the interval needs to be long enough to include sufficient data, typically between 5 and 10 times the spin period of the measured source.

Following Bildsten et al. (1997) and Woods et al. (2007), the GBM pulsed flux (F_{pulsed}) is obtained as the rms pulsed flux:

$$F_{\text{pulsed}} = \sqrt{\sum_{h=1}^N \frac{a_h^2 + b_h^2 - (\sigma_{a_h}^2 + \sigma_{b_h}^2)}{2}} \quad (19)$$

where

$$\sigma_{a_h}^2 = \frac{4}{P^2} \sum_{i=1}^P \sigma_{r_i}^2 \cos^2(2\pi\phi_i h), \quad \sigma_{b_h}^2 = \frac{4}{P^2} \sum_{i=1}^P \sigma_{r_i}^2 \sin^2(2\pi\phi_i h) \quad (20)$$

and P is the total number of phase bins, and σ_{r_i} is the uncertainty in the count rate in the i th phase bin. The spectral model used to combine the count rate of each source with the spectral response is an empirical model based on observations published in the literature. This procedure ensures that the pulsed flux is unbiased against the energy dependence of pulsed flux commonly observed in accreting XRPs, because the F_{pulsed} is calculated in relatively narrow energy bins, and the effect of an incorrectly assumed spectral model has been

calculated to affect the derived flux only marginally, i.e., at a $\sim 5\%$ level (Wilson-Hodge et al. 2012).

4.4. Pulse Profiles Using a Search in Frequency and Frequency Derivative

Due to the spin evolution shown by accreting pulsars, it is useful to apply a technique that not only estimates the spin frequency but also its derivative. Consequently, a search over a grid of pulse frequencies and frequency derivatives is performed to find the best-fitting value. The search range is often estimated using past measurements (depending on availability); otherwise, a safe interval of $\pm 0.01\nu_0$ is used (where ν_0 is the pulsar frequency estimated in Section 4.3). For an estimation of the pulsar frequency derivative range, a maximum spin-up rate is obtained from accretion theory (e.g., Parmar et al. 1989) assuming canonical NS parameters,

$$\dot{\nu} = 1.9 \times 10^{-12} \mu_{30}^{2/7} L_{37}^{6/7} \text{ Hz s}^{-1}, \quad (21)$$

where μ_{30} is the magnetic moment of the NS in units of 10^{30} G cm^3 , and L_{37} is the luminosity in units of $10^{37} \text{ erg s}^{-1}$. Typical spin-down rates are of the order of a few times $10^{-13} \text{ Hz s}^{-1}$. Equation (21) is considered applicable only on a limited range of relatively high-luminosity values (Parmar et al. 1989), a condition that is met for all analyzed sources when detected by GBM.

Once the frequency and frequency derivative search ranges are established, a grid of phase offsets from the phase model in Equation (16) is created

$$\delta\phi_k(\delta\nu, \dot{\nu}_q) = \delta\nu_p(\bar{t}_k - \tau) + \frac{1}{2}\dot{\nu}_q(\bar{t}_k - \tau)^2, \quad (22)$$

where \bar{t}_k is the time at the midpoint of segment k , τ is a reference epoch chosen near the center of the considered time interval (that is, at epoch τ , $\delta\phi = 0$ by definition), $\delta\nu_p$ is an offset in pulse frequency from ν_0 in Equation (17), and $\dot{\nu}_q$ is its derivative. Each offset in pulse phase leads to a shift in the individual pulse profiles, applied as a modification of the estimated complex Fourier coefficient:

$$\beta_{kh}(\delta\nu, \dot{\nu}_q) = (a_{kh} - i b_{kh}) \exp \{-i 2\pi h \delta\phi(\delta\nu, \dot{\nu}_q)\}, \quad (23)$$

where a_{kh} and b_{kh} are the harmonic coefficients for harmonic h and profile k from Equation (16). The best frequency and frequency derivative within the search grid were determined using the Y_n statistic, following Finger et al. (1999).

4.5. Phase Offset Estimation and Model Fitting

Once pulse profile templates are obtained following the methods outlined in Sections 4.3 and 4.4, a phase offset $\Delta\phi$ can be estimated by comparing the fitted pulse profiles with the obtained template. The $\Delta\phi$ and pulse amplitude A of each pulse is then determined by fitting each pulse profile to the template (T_h) by minimization of

$$\chi^2 = \sum_{k=1}^M \frac{|\alpha_{kh} - A T_h \exp(-i 2\pi h \Delta\phi_k)|^2}{\sigma_{kh}^2}. \quad (24)$$

Here, $\alpha_{kh} = a_{kh} - i b_{kh}$ is the complex Fourier coefficient for harmonic h and profile k , and σ_{kh}^2 is the error on the real or imaginary component of α_{kh} .

Phase offsets are the signature that the observed spin frequency is modulated by some effect. If the offsets present a random, erratic behavior consistent with a constant value, then the phase model cannot be improved, and the offsets are considered noise. However, if the offsets show a (possibly periodic) pattern, the phase model can be improved by minimization of

$$\chi^2 = \sum_{k=1}^M \frac{(\phi(t_k^{\text{em}}) - \phi^{\text{model}}(t_k^{\text{em}}))^2}{\sigma_{\phi(t_k^{\text{em}})}^2}, \quad (25)$$

where $\phi(t_k^{\text{em}})$ is the total measured pulse phase (the phase model used to fold the pulse profiles plus the measured offset), $\sigma_{\phi(t_k^{\text{em}})}^2$ is the error on $\phi(t_k^{\text{em}})$, and $\phi^{\text{model}}(t_k^{\text{em}})$ is the new phase model that has been used in the fit. Typically, the Levenberg-Marquardt method (Press et al. 1992) is used for the minimization of Equation (25). Such a process constrains the pulsar binary orbit by considering $t^{\text{em}} = \text{TDB} - z$, remembering that TDB is the Dynamical Barycentric Time and z is the line-of-sight delay associated with the binary orbit (see Section 4.1 and Equation (14)).

5. Overview of Accreting X-Ray Pulsars

XRP that are part of binary systems can be classified into two groups, according to the mass of the donor star (Lewin et al. 1997):

1. High Mass X-ray Binaries (HMXBs) are systems where the donor star is a massive O or B stellar type, typically with $M \geq 5 M_{\odot}$. The system is generally younger, and the stellar wind is strong. When the compact object is an NS, its magnetic field is of the order of 10^{12} G. In our Galaxy, these objects are mostly found on the Galactic plane, especially along the spiral arms.
2. Low Mass X-ray Binaries (LMXBs) are systems where the donor star is a spectral type A or later star, or a white dwarf with a mass of $M \leq 1.2 M_{\odot}$. These systems are generally older than HMXBs, with weaker stellar winds from the donor. The NS magnetic field observed in these systems has decayed to about 10^{7-8} G. Moreover, LMXBs are typically found toward the Galactic center; although, some of them have been observed in globular clusters.

XRPs are largely found in HMXBs. In fact, GBM detected XRPs are almost exclusively HMXBs. Depending on the binary system properties, three different methods of mass transfer can take place in X-ray binaries:

1. *Wind-fed systems*. Accretion from stellar winds is particularly relevant when the donor star is a massive main-sequence or supergiant O/B star, because those winds are dense, with mass-loss rates of $\dot{M}_w \approx 10^{-6}-10^{-7} M_{\odot} \text{ yr}^{-1}$. Typically, in wind-fed systems, the compact object orbits the donor star at a close distance, thus, being deeply embedded in the stellar wind, accreting at all orbital phases. These systems are therefore *persistent* sources, showing variability on a timescale that is much shorter than the orbital period (i.e., 10^2-10^4 s).
2. *Roche lobe-overflow (RLO) systems*. When the binary system is such that the donor star radius is larger than its Roche lobe, the star loses part of its material through the first Lagrangian point L_1 . When RLO takes place, the

mass flow does not directly impact the compact object due to the intrinsic orbital angular momentum of the transferred material. Instead, it forms an accretion disk around the compact object. Since the transfer of matter is generally steady, RLO systems are also persistent sources.

3. *Be/X-Ray Binary systems (BeXRBs)*. In these systems, the donor star is an O- or B-type star that expels its wind on the equatorial plane under the form of a circumstellar disk (also called the Be disk). The disk is composed of ionized gas that produces emission lines (especially H α). When the orbiting compact object (CO) passes close to or through the Be disk, a large flow of matter is pulled from the disk, forming an accretion disk around the CO by its gravitational potential. Subsequently, matter is then accreted onto the CO giving rise to an X-ray outburst. Due to the orbital modulation of the accreted matter, these systems show only *transient* activity. X-ray outbursts in BeXRBs are classified into two types:
 - (a) Type I: also called *normal* outbursts. These are less luminous outbursts, with a peak luminosity of $\sim 10^{36-37} \text{ erg s}^{-1}$, occurring typically at periastron passages and lasting for a fraction of the orbital period.
 - (b) Type II: also called *giant* outbursts. These episodes are more rare, more luminous (peak luminosity of $\sim 10^{37-38} \text{ erg s}^{-1}$), and do not show any preferred orbital phase, lasting for a large fraction of the orbital period or even for several orbits.

Despite the aforementioned classifications, the zoo of XRPs often shows systems that have properties belonging to different classes and are characterized by mixed mass transfer modalities. For example, theoretical and observational works show that wind-captured disks can form around the CO of certain HMXBs (see, e.g., Jenke et al. 2012b; Blondin 2013; El Mellah et al. 2019). Moreover, the recent discovery of new systems led to the classification of additional subclasses, e.g., the HMXBs with supergiant companions (SgXBs), and the Super-giant Fast X-ray Transients (SFXTs; Sidoli & Paizis 2018, and references therein). However, different subclasses may also represent similar systems observed at different accretion regimes or at different evolutionary stages. For example, gated accretion models are invoked to explain the variable activity of SFXTs, where the transitions between possible regimes are triggered by the inhomogeneous (i.e., clumpy) ambient wind (Bozzo et al. 2016; Martínez-Núñez et al. 2017; Pradhan et al. 2018, and references therein).

All GBM detected XRPs and relevant properties are summarized in Table 1. The different classes for these sources are shown in Figure 1, where they are plotted in the Corbet diagram (Corbet 1986).

6. Individual Accreting X-Ray Pulsars Observed by GBM

There are 39 sources in total, 31 transient systems, and eight persistent systems, with frequency and pulsed flux histories available on the GAPP public website.¹⁰ For each source, we link the corresponding GAPP web page for the reader's convenience. The main properties of each source are listed in Table 1, along with their distance values as measured either by

¹⁰ <https://gammaray.nsstc.nasa.gov/gbm/science/pulsars.html#>

Table 1
GBM X-Ray Pulsars: Coordinates, Orbital Elements, Spin Periods, and Distances

Source	Class	R.A. ($^{\circ}$)	Decl. ($^{\circ}$)	P_{orb} (days)	P_{spin} (s)	$T_{\pi/2}$ (MJD)	$a_s \sin i$ (l s)	w ($^{\circ}$)	e	d^{\dagger} (kpc)
<i>Transient</i>										
GRO J1744–28 (Sanna et al. 2017)	LMXB-RLO	266.1379	−28.7408	11.8358(5)	0.467046314	56692.739(2)	2.639(1)	0.00	$<6 \times 10^{-3}$	$8.5^{+2.0}_{-4.5}$ (Nishiuchi et al. 1999)
SAX J2103.5+4545 (Camero Arranz et al. 2007)	BeXRB	315.8988	45.7515	12.66528(51)	358.61	52545.411(24)	80.81(67)	241.36(2.18)	0.401(18)	$6.4^{+0.9}_{-0.7}$
4U 1901+03 (Galloway et al. 2005; Jenke & Finger 2011; this work)	BeXRB	285.9047	3.1920	22.5348(21)	2.761792	58563.8361(8)	106.989(15)	268.812(3)	0.0363(3)	$2.2^{+2.2}_{-1.3}$
RX J0520.5–6932 (Kuehnel et al. 2014)	BeXRB	80.1288	−69.5319	23.93(7)	8.037	56666.41(3)	107.6(8)	233.50	0.0286	LMC
A 1118-615 (Staubert et al. 2011)	BeXRB	170.2408	−61.9161	24.0(4)	407.6546	54845.37(10)	54.8(1.4)	310(30)	0.10(2)	$2.93^{+0.26}_{-0.22}$
4U 0115+63 (this work)	BeXRB	19.6329	63.7400	24.316895	3.61	57963.237(3)	141.769(72)	49.51(9)	0.3395(2)	$7.2^{+1.5}_{-1.1}$
Swift J0513.4–6547 (Coe et al. 2015)	BeXRB	78.3580	−65.7940	27.405(8)	27.28	54899.02(27)	191(13)	...	<0.17	LMC
Swift J0243.6+6124 Jenke et al. (2018b)	BeXRB	40.9180	61.4341	27.587(17)	9.86	58103.129(17)	115.84(32)	−73.56(16)	0.09848 (42)	$6.9^{+1.6}_{-1.2}$
GRO J1750–27 (Scott et al. 1997, with period correction from GBM data)	BeXRB	267.3046	−26.6437	29.803890	4.45	49931.02(1)	101.8(5)	206.3(3)	0.360(2)	$18.0^{+4.0}_{-4.0}$ (Lutovinov et al. 2019)
Swift J005139.2–721704 (Laycock et al. 2003)	BeXRB	12.9116	−72.284666	20–40	4.8	SMC
2S 1553–542 (this work)	BeXRB	239.4542	−54.4150	31.34(1)	9.29	57088.927(4)	201.48(25)	164.8(1.2)	0.0376(9)	$20.0^{+4.0}_{-4.0}$ (Tsygankov et al. 2016)
V 0332+53 (Doroshenko et al. 2016)	BeXRB	53.7495	53.1732	33.850(3)	4.37	57157.38(5)	77.8(2)	277.4(1)	0.371(5)	$5.1^{+1.1}_{-0.8}$
XTE J1859+083 (Kuehnel 2016)	BeXRB	284.7700	8.2500	37.97	10.0	57078.7	57100.5(5)	211.4(1.8)	−117.0 (0.9)	$2.7^{+2.4}_{-1.5}$
KS 1947+300 (Galloway et al. 2004)	BeXRB	297.3979	30.2088	40.415(10)	18.81	51985.31(7)	137(3)	33(3)	0.033(13)	$15.2^{+3.7}_{-2.8}$
2S 1417–624 (Finger et al. 1996a; İnam et al. 2004)	BeXRB	215.3000	−62.7000	42.19(1)	17.51	51612.17(5)	188(2)	300.3(6)	0.446(2)	$3.8^{+7.8}_{-1.8}$
SMC X-3 (Townsend et al. 2017)	BeXRB	13.0237	−72.4347	45.04(8)	7.81	57676.4(3)	190.3(1.3)	240.3(1.1)	0.244(5)	SMC
EXO 2030+375 (Wilson et al. 2008)	BeXRB	308.0633	37.6375	46.0213(3)	41.33	52756.17(1)	246(2)	211.9(4)	0.410(1)	$3.6^{+1.4}_{-0.9}$
MXB 0656–072 (Morgan et al. 2003)	BeXRB	104.6125	−7.2633	101.2	160.7	0.4 (Yan et al. 2012)	$5.1^{+1.4}_{-1.0}$
GS 0834–430 (Wilson et al. 1997)	BeXRB	128.9792	−43.1850	105.8(4)	12.3	(0.10–0.17)	$5.5^{+2.5}_{-1.7}$
GRO J2058+42 (Wilson et al. 1998)	BeXRB	314.6987	41.7743	110(3)	193.61	$8.0^{+1.2}_{-1.0}$
A 0535+26 (Finger et al. 1996c)	BeXRB	84.7274	26.3158	111.1(3)	103.5	49156.7(1.0)	267(13)	130(5)	0.42(2)	$2.13^{+0.26}_{-0.21}$
IGR J19294+1816 (Corbet & Krimm 2009)	BeXRB	292.4829	18.3107	117.2 or 22.25 (Cusumano et al. 2016)	12.45	$2.9^{+2.5}_{-1.5}$
GX 304-1 (Sugizaki et al. 2015)	BeXRB	195.3213	−61.6018	132.18900	272.0	55425.6(5)	601(38)	130(4)	0.462(19)	$2.01^{+0.15}_{-0.13}$
RX J0440.9+4431 (Ferrigno et al. 2013)	BeXRB	70.2472	44.5304	150.0(2)	202.5	>0.4 (Yan et al. 2016)	$3.2^{+0.7}_{-0.5}$
XTE J1946+274 (Marcu-Cheatham et al. 2015)	BeXRB	296.4140	27.3654	172.7(6)	15.74974	55515.0(1.0)	471.2(4.3)	−87.4(1.7)	0.246(9)	$12.6^{+3.9}_{-2.9}$ (Orlandini et al. 2012)
2S 1845–024 (Finger et al. 1999)	BeXRB	282.0738	−2.4203	242.180(12)	94.6	49616.48(12)	689(38)	252(9)	0.8792(54)	$10.0^{+2.5}_{-2.5}$ (Koyama et al. 1990)
GRO J1008–57 (Coe et al. 2007; Kühnel et al. 2013)	BeXRB	152.4420	−58.2933	249.48(4)	93.7134	54424.71(20)	530(60)	−26(8)	0.68(2)	$5.8^{+0.5}_{-0.5}$ (Riquelme et al. 2012)
Cep X-4 (Wilson et al. 1999)	BeXRB	324.8780	56.9861	(23-147)	66.3	$10.2^{+2.2}_{-1.6}$
IGR J18179–1621 (Halpern 2012)	HMXB	274.4675	−16.3589	...	11.82	$8.0^{+2.0}_{-7.0}$ (Nowak et al. 2012)
MAXI J1409–619 (Kennea et al. 2010)	BeXRB?	212.0107	−61.9834	...	506	$14.5^{+2.0}_{-2.0}$ (Orlandini et al. 2012)
XTE J1858+034 (Remillard et al. 1998)	BeXRB	284.6780	3.4390	...	221.0	$1.55^{+0.28}_{-0.21}$

Table 1
(Continued)

Source	Class	R.A. ($^{\circ}$)	Decl. ($^{\circ}$)	P_{orb} (days)	P_{spin} (s)	$T_{\pi/2}^e$ (MJD)	$a_s \sin i$ (l s)	w ($^{\circ}$)	e	d^{\dagger} (kpc)
4U 1626–67 (Chakrabarty 1998)	LMXB —RLO	248.0700	−67.4619	0.02917(3)	<i>Persistent</i> 7.66	$3.5^{+2.3}_{-1.3}$
Her X-1 (Staubert et al. 2009)	LMXB —RLO	254.4571	35.3426	1.700167590(2)	1.237	46359.871940(6)	13.1831(4)	96.0(10.0)	4.2(8)E-4	$5.0^{+0.8}_{-0.6}$
Cen X-3 (Raichur & Paul 2010b; Falanga et al. 2015)	sgHMXB —RLO + wind	170.3133	−60.6233	2.08704106(3)	4.8	50506.788423(7)	39.6612(9)	...	<0.0001	$6.4^{+1.4}_{-1.1}$
4U 1538–52 (Falanga et al. 2015; Clark 2000)	sgHMXB —wind	235.5971	−52.3861	3.7284140(76)	526.8	52 855.061(13)	53.1(1.5)	40(12)	0.17(1)	$6.6^{+2.2}_{-1.5}$
Vela X-1 (Bildsten et al. 1997; Kreykenbohm et al. 2008; Falanga et al. 2015)	sgHMXB —wind	135.5286	−40.5547	8.964427(12)	83.2	42 611.349(13)	113.89(13)	152.59(92)	0.0898(12)	$2.42^{+0.19}_{-0.17}$
8 OAO 1657–415 (Jenke et al. 2012b; Falanga et al. 2015)	sgHMXB —wind	255.2038	−41.6560	10.447355(92)	37.1	52674.1199(17)	106.157(83)	92.69(67)	0.1075(12)	7.1 ± 1.3 (Audley et al. 2006)
GX 301-2 (Sato et al. 1986; Koh et al. 1997; Doroshenko et al. 2010a)	hgHMXB —wind	186.6567	−62.7703	41.506(3)	684.1618	53532.15000	368.3(3.7)	310.4(1.4)	0.462(14)	$3.5^{+0.6}_{-0.5}$
GX 1+4 (Hinkle et al. 2006)	LMXB	263.0128	−24.7456	1160.8(12.4)	159.7	51942.5(53.0)	773(20)	168(17)	0.101(22)	$7.6^{+4.3}_{-2.8}$

Note. Sources are listed from top to bottom in order of increasing orbital period. * Mid-eclipse time, equivalent to the time when the mean longitude $l = \pi/2$ for a circular orbit;[†] Distances obtained from the second Gaia Data Release (DR2; unless specified otherwise); Large and Small Magellanic Clouds (LMC and SMC) are considered at 50 and 62 kpc, respectively. The sources from which spectral models, orbital parameters, and distances for targets unavailable in the Gaia DR2 are obtained are cited where applicable.

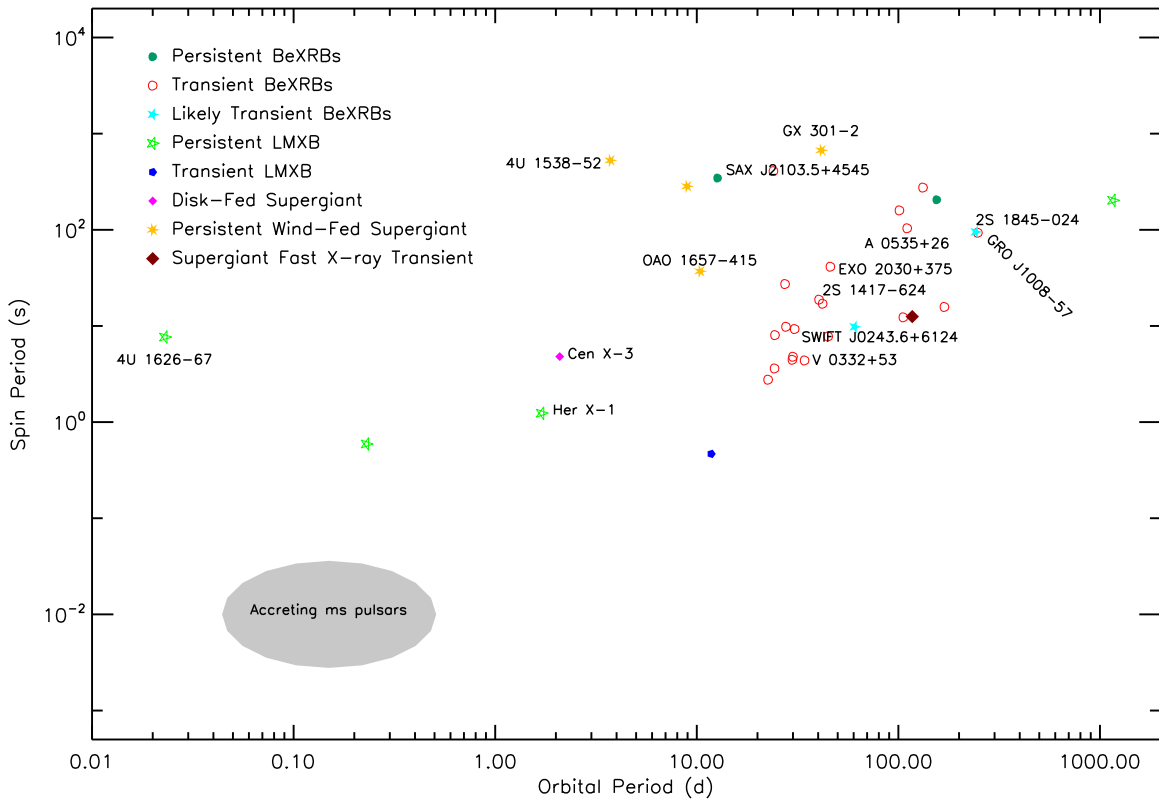


Figure 1. Corbet diagram showing spin period (y-axis) vs. orbital period (x-axis) for all GBM detected accreting XRBs with known orbital period. A few representative sources have been labeled. The region populated by accreting millisecond pulsars (shown by the gray oval) has also been labeled for comparison.

Gaia (Bailer-Jones et al. 2018) following the method described in Appendix B or as otherwise specified.

6.1. Transient Outbursts in BeXRB Systems

Most GBM detected XRBs are BeXRB systems. Among the transient systems, pulsations from 28 BeXRBs, 1 possible BeXRB, 1 HXMB (with no better subclassification), and 1 LMXB are observed with GBM. Below, we describe the main timing properties of each transient XRB detected by GBM.

6.1.1. GRO J1744–28

GRO J1744–28 is the fastest accreting X-ray pulsar, with a spin period of only ~ 44 ms, discovered with BATSE (Finger et al. 1996a). This source is also known as the *Bursting Pulsar*, due to the fact that it shows Type II–like bursting activity, usually attributed to thermonuclear burning, but it is possibly due to accretion processes in GRO J1744–28 (Court et al. 2018 and references therein). It is the only LMXB among the transient systems detected by GBM. It has an orbital period of about 12 days, and its distance is calculated as ~ 8.5 kpc in Kouveliotou et al. (1996) and Nishiuchi et al. (1999), but it is challenged by the value of ~ 4 kpc obtained from studies of its near-infrared counterpart, a reddened K2 III giant star (Gosling et al. 2007; Wang et al. 2007; Masetti et al. 2014). On the other hand, the closest Gaia counterpart is located at $14''$ from the nominal source position and at a distance of $1.3^{+1.2}_{-0.5}$ kpc. The activity observed from GRO J1744–28 is limited to three episodes: the Type II outburst that led to its discovery in 1995 (Kouveliotou et al. 1996), the outburst that occurred in 1997 (Nishiuchi et al. 1999), and the last one in 2014, which followed almost two decades of quiescence (D’Ài et al. 2015;

Sanna et al. 2017 and references therein). The spin-up rate observed during the outbursts is of the order of $10^{-12} \text{ Hz s}^{-1}$, while the secular spin-up trend shows an average rate of about $2 \times 10^{-13} \text{ Hz s}^{-1}$ (Sanna et al. 2017). GBM also measured an average value of the spin derivative of $\sim 3 \times 10^{-12} \text{ Hz s}^{-1}$ during the 2014 outburst.¹¹ Comparisons with archival BATSE data show a marginal long-term spin-up trend with an average rate of $\dot{\nu} \sim 1 \times 10^{-14} \text{ Hz s}^{-1}$.

6.1.2. SAX J2103.5+4545

SAX J2103.5+4545 was discovered by BeppoSAX as a transient accreting pulsar with a spin period of ~ 360 s (Hulleman et al. 1998). With an orbital period of ~ 13 days, it is among the shortest known for a BeXRB (Baykal et al. 2007). The Gaia distance for this source is $6.4^{+0.9}_{-0.7}$ kpc, consistent with the distance value obtained from optical observations of the B0 Ve companion star (6.5 kpc; Reig et al. 2004b, 2010). Although SAX J2103.5+4545 has been classified as a BeXRB (Reig et al. 2004b), it does not follow the Corbet $P_{\text{orb}}-P_{\text{spin}}$ correlation, but it is located in the region of wind accretors (see Figure 1). Since its discovery, numerous Type I and Type II outbursts have been observed (Camero Arranz et al. 2007). Since then, SAX J2103.5+4545 has been showing a general spin-up trend at different rates¹² but with an average value of $\dot{\nu} \approx 10^{-12} \text{ Hz s}^{-1}$ (Camero Arranz et al. 2007). Those authors also observe a spin-up rate steeper than the expected power-law correlation, with a $6/7$ index as

¹¹ <https://gammaray.nsstc.nasa.gov/gbm/science/pulsars/lightcurves/groj1744.html>

¹² <https://gammaray.nsstc.nasa.gov/gbm/science/pulsars/lightcurves/saxj2103.html>

reported in Equations (10) and (21) (see Figure 13 in their work). During outburst episodes, the measured spin-up rate is $\dot{\nu} = -2.6 \times 10^{-12} \text{ Hz s}^{-1}$ (Ducci et al. 2008). However, long (\sim yr) spin-down periods have also been observed between outbursts, with $\dot{\nu} = 4.2 \times 10^{-14} \text{ Hz s}^{-1}$ (Ducci et al. 2008).

6.1.3. 4U 1901+03

4U 1901+03 was first detected in X-rays by the Uhuru mission in 1970–1971 (Forman et al. 1976). Afterwards, the source remained undetected until 2003, when it underwent a Type II outburst that lasted for about 5 months and during which pulsations were detected at a spin period of about 3 s (Galloway et al. 2005). The orbital period is \sim 23 days (Galloway et al. 2005; Jenke & Finger 2011). The optical companion stellar type was uncertain until recent measurements were obtained by McCollum & Laine (2019), who proposed a B8/9 IV star, which is consistent with the X-ray timing analysis that favors a BeXRB nature (Galloway et al. 2005). The Gaia measured distance is $2.2^{+2.2}_{-1.3} \text{ kpc}$, much closer than the initially proposed distance of \sim 10 kpc (Galloway et al. 2005). However, optical spectroscopy of the optical companion, together with the separation between the Gaia measurement and the Chandra derived position for this source (Halpern & Levine 2019), led Strader et al. (2019) to favor a distance $>12 \text{ kpc}$ for this system. After the Type II outburst in 2003, the source has remained mostly quiescent, showing moderate activity in 2011 December (Jenke & Finger 2011; Sootome et al. 2011), when a weak flux increase was observed, accompanied by a spin-up trend. The spin-up observed during the Type II outburst in 2003 was $2.9 \times 10^{-11} \text{ Hz s}^{-1}$ (Galloway et al. 2005). More recently however, the source underwent another Type II outburst (Kennea et al. 2019; Nakajima et al. 2019). The GBM spin-up average rate¹³ measured during the 2019 outburst episode was $1.4 \times 10^{-11} \text{ Hz s}^{-1}$, similar to that of the previous Type II outburst. GBM also observed the source slowly spinning down between outbursts at an average rate of $4.2 \times 10^{-13} \text{ Hz s}^{-1}$.

6.1.4. RX J0520.5–6932

RX J0520.5–6932 was discovered with ROSAT (Schmidtke et al. 1994). The only pulsations were detected two decades later, when a Swift/XRT survey of the LMC in 2013 revealed RX J0520.5–6932 to have undergone an X-ray outburst, and XMM-Newton observations found a spin period of about 8 s (Vasilopoulos et al. 2014). The orbital period is \sim 24 days (Coe et al. 2001; Kuehn et al. 2014). The optical counterpart is an O9 Ve star (Coe et al. 2001), and the source is located in the LMC (\sim 50 kpc). The outburst observed in 2013 was the first and only one since its discovery (Vasilopoulos et al. 2013). During that episode, a strong spin-up trend was observed by GBM,¹⁴ at a rate of $\dot{\nu} = 3.5 \times 10^{-11} \text{ Hz s}^{-1}$.

6.1.5. A 1118–616

X-ray pulsations with a period of 406.5 s were discovered in A 1118–616 by Ariel 5. Initially interpreted as the binary period (Ives et al. 1975), it was later identified as the pulsar

spin period (Fabian et al. 1975, 1976). The first determination of the orbital period of 24 days was obtained later by Staubert et al. (2011). The optical companion is an O9.5 IV–Ve star, Hen 3-640/Wray 793 (Chevalier & Ilovaisky 1975), and the Gaia measured distance for this system is $2.9^{+0.3}_{-0.2} \text{ kpc}$ (although, other works locate it at about 5.2 kpc; Janot-Pacheco et al. 1981; Riquelme et al. 2012). Its outburst activity is sporadic, with only three major outbursts since its discovery (see Suchy et al. 2011 and references therein). The average spin-up rate observed during accretion is of the order of $(2\text{--}4) \times 10^{-13} \text{ Hz s}^{-1}$ (see, e.g., Coe et al. 1994b, and the relevant GAPP web page¹⁵), while the secular trend between outbursts is a spin-down rate of about $-9.1 \times 10^{-14} \text{ Hz s}^{-1}$ (Mangano 2009; Doroshenko et al. 2010b). After the 2011 outburst, the source entered a quiescent period that is still ongoing at the time of writing, remaining undetected with GBM.

6.1.6. 4U 0115+634

Pulsations at \sim 4 s from 4U 0115+634 were discovered by SAS-3 in 1978 (Cominsky et al. 1978). The orbital period is 24 days (Rappaport et al. 1978), and the optical companion is V635 Cas, a B0.2 Ve star. It has a Gaia measured distance of $7.2^{+1.5}_{-1.1} \text{ kpc}$, consistent with the approximate value of \sim 7 kpc inferred by Negueruela & Okazaki (2001) and Riquelme et al. (2012). 4U 0115+634 shows frequent outburst activity, with Type II outbursts observed as often as Type I outbursts, at a quasi-periodicity of 3–5 yr (Negueruela & Okazaki 2001; Negueruela et al. 2001). The general spin period evolution trend shows spin-down during quiescence, as well as between outbursts. However, rapid spin-up episodes are observed during Type II activity, $\dot{\nu} \sim 2.3 \times 10^{-11} \text{ Hz s}^{-1}$ (Li et al. 2012). This resulted in a secular spin-up trend (Boldin et al. 2013). However, the secular trend has recently inverted, and the source started to show long-term spin-down as observed by GBM.¹⁶

6.1.7. Swift J0513.4–6547

Swift J0513.4–6547 was discovered by Swift during an outburst and identified as a pulsar with a spin period of 28 s in the same observation (Krimm et al. 2009). The outburst lasted for about 2 months, after which the source entered quiescence interrupted only by a moderate re-brightening in 2014, when it showed a luminosity of the order of $10^{36} \text{ erg s}^{-1}$ (Sturm et al. 2014; Şahiner et al. 2016). The system is located in the LMC, and the optical companion is a B1 Ve star (Coe et al. 2015). The peak spin-up rate observed by GBM¹⁷ during the 2009 outburst is about $3 \times 10^{-10} \text{ Hz s}^{-1}$ (Finger & Beklen 2009; Coe et al. 2015), while during the quiescent period between 2009 and 2014, the source was spinning down at an average rate of $-1.5 \times 10^{-12} \text{ Hz s}^{-1}$ (Şahiner et al. 2016).

6.1.8. Swift J0243.6+6124

Swift J0243.6+6124 is the newest discovered source in the present catalog and among the brightest. It was first discovered by Swift and then independently identified as a pulsar by Swift

¹³ <https://gammaray.nsstc.nasa.gov/gbm/science/pulsars/lightcurves/4u1901.html>

¹⁴ <https://gammaray.msfc.nasa.gov/gbm/science/pulsars/lightcurves/rxj0520.html>

¹⁵ <https://gammaray.nsstc.nasa.gov/gbm/science/pulsars/lightcurves/a1118.html>

¹⁶ <https://gammaray.nsstc.nasa.gov/gbm/science/pulsars/lightcurves/4u0115.html>

¹⁷ <https://gammaray.nsstc.nasa.gov/gbm/science/pulsars/lightcurves/swiftj0513.html>

and GBM, with a spin period of about 10 s (Jenke & Wilson-Hodge 2017; Kennea et al. 2017). The orbital period is ~ 27 days (Jenke et al. 2018b), and the optical counterpart is a late Oe-type or early Be-type star (Bikmaev et al. 2017), with a Gaia measured distance of $6.9^{+1.6}_{-1.2}$ kpc. Following its discovery, the source entered a Type II outburst that lasted for ~ 150 days, becoming the first known galactic Ultra-Luminous X-ray (ULX) pulsar, with a peak luminosity of about 2×10^{39} erg s $^{-1}$ (Wilson-Hodge et al. 2018). During the outburst episode, the source showed dramatic spin-up at a maximal rate of $\sim 2 \times 10^{-10}$ Hz s $^{-1}$ (Doroshenko et al. 2017). After the Type II outburst, the source kept showing weaker X-ray activity for a few of the following periastron passages.¹⁸ During these later passages, the spin-down rate of the source was about 100 times slower ($\sim -2 \times 10^{-12}$ Hz s $^{-1}$), even at an accretion luminosity of a few 10^{36} erg s $^{-1}$ (Doroshenko et al. 2020; Jaisawal et al. 2019). Only during the last exhibited outburst did the source show a spin-up trend again at a rate comparable to the previously observed spin-up phase. Currently, the source remains quiescent.

6.1.9. GRO J1750–27

Pulsations at 4 s from GRO J1750–27 were observed by BATSE during the same outburst that led to its discovery (Wilson et al. 1995; Scott et al. 1997). The orbital period is about 30 days, and the system is located at a distance of ~ 18 kpc (Scott et al. 1997; Lutovinov et al. 2019), with no Gaia DR2 counterpart (but with a DR1 solution of $1.4^{+1.9}_{-0.5}$ kpc). No optical counterpart has been identified yet due to the location of the system beyond the Galactic center. However, following the classification of Corbet (1986), Scott et al. (1997) identified GRO J1750–27 as a BeRXB. GRO J1750–27 shows only sporadic outburst activity, with only three outbursts detected since its discovery and only one observed by GBM.¹⁹ Local spin-up trends during these outbursts have been observed at a rate of about 1.5×10^{-11} Hz s $^{-1}$ (Shaw et al. 2009; Lutovinov et al. 2019). The source does not show any appreciable spin derivative during quiescent periods.

6.1.10. Swift J005139.2–721704

Pulsations at about 4.8 s were first discovered from the SMC source XTE J1858+034 with RXTE (Corbet et al. 2001). This source has recently been identified as coincident with Swift J005139.2–721704 in the SMC (Strohmayer et al. 2018) and is listed on the GAPP website with this name.²⁰ Laycock et al. (2003) identified the source as a BeXRB, inferring its orbital period as ~ 20 –40 days based on its pulsation period and its possible location on the Corbet diagram. Pulsations from this source were observed with GBM only once, during its recent outburst in 2018. This represented only the second outburst ever observed from this source (Monageng et al. 2019 and references therein). These authors reported the source to show unusual spin-down trends during accretion, which may be due to orbital modulation.

6.1.11. 2S 1553–542

Pulsations at ~ 9 s from 2S 1553–542 were discovered by SAS-3 (Kelley et al. 1982). The orbital period is about 31 days (Kelley et al. 1983a), and the optical companion has been identified as a B1-2V type star (Lutovinov et al. 2016). The closest counterpart measured by Gaia is located at an angular offset of $17''.3$ from the nominal source position, at a distance of $3.5^{+2.6}_{-1.5}$ kpc. However, a distance of 20 ± 4 kpc has been reported by Tsygankov et al. (2016) based on the assumption of accretion-driven spin-up. Since its discovery, the source has exhibited three outbursts, all of which were Type II (see Tsygankov et al. 2016 and references therein). This behavior is interpreted in terms of the low eccentricity ($e \sim 0.035$) of the binary orbit (Okazaki & Negueruela 2001). Local spin-up rates during accretion episodes were measured as 2.9×10^{-11} Hz s $^{-1}$ for the 2008 outburst (Pahari & Pal 2012) and 8.7×10^{-12} Hz s $^{-1}$ for the 2015 outburst.²¹ The spin-down rate measured between these outbursts is about -4.0×10^{-13} Hz s $^{-1}$ (Tsygankov et al. 2016).

6.1.12. V 0332+53

Pulsations at ~ 4 s from V 0332+53 were detected by the EXOSAT satellite (Stella et al. 1985). The same observations revealed a moderately eccentric orbit ($e \sim 0.3$) and an orbital period of about 34 days. The optical companion is an O8-9 Ve star, BQ Cam (Honeycutt & Schlegel 1985; Negueruela et al. 1999), and the system distance was first estimated to be 2.2–5.8 kpc (Corbet et al. 1986). This was later increased to 6–9 kpc (Negueruela et al. 1999). Both findings are consistent with a Gaia measured distance of $5.1^{+1.1}_{-0.8}$ kpc. Since its discovery, the source has shown four Type II outbursts, each one lasting for a few orbital periods and reaching peak luminosities of $\sim 10^{38}$ erg s $^{-1}$ (see Doroshenko et al. 2016 and references therein). The spin-up rate measured during outburst episodes is $(2-3) \times 10^{-12}$ Hz s $^{-1}$ (Raichur & Paul 2010a). However, as outburst activity from this source is relatively rare, the net secular spin derivative trend shows a slow spin-down,²² $\sim -5 \times 10^{-14}$ Hz s $^{-1}$.

6.1.13. XTE J1859+083

Pulsations from XTE J1859+083 at ~ 10 s were discovered with RXTE (Marshall et al. 1999). An orbital period of 60.6 days was first proposed by Corbet et al. (2009), based on the separation of a few outbursts. However, analysis of a series of outbursts in 2015 led to a refined orbital solution with an orbital period of 37.9 days (Kuehnel 2016). No optical companion has been identified yet, but the source is considered a BeXRB due to its position on the Corbet diagram. The closest counterpart measured by Gaia is located at an angular offset of $17''.3$, at a distance of $2.7^{+2.4}_{-1.5}$ kpc. In 2015, the source showed a new bright outburst (Finger et al. 2015 and references therein), during which GBM²³ measured a strong spin-up rate of $\dot{\nu} \sim 1.6 \times 10^{-11}$ Hz s $^{-1}$, similar to the rate observed in 1999 (Corbet et al. 2009).

¹⁸ <https://gammaray.nsstc.nasa.gov/gbm/science/pulsars/lightcurves/swiftj0243.html>

¹⁹ <https://gammaray.msfc.nasa.gov/gbm/science/pulsars/lightcurves/groj1750.html>

²⁰ <https://gammaray.nsstc.nasa.gov/gbm/science/pulsars/lightcurves/swiftj005139.html>

²¹ <https://gammaray.msfc.nasa.gov/gbm/science/pulsars/lightcurves/2s1553.html>

²² <https://gammaray.nsstc.nasa.gov/gbm/science/pulsars/lightcurves/v0332.html>

²³ <https://gammaray.msfc.nasa.gov/gbm/science/pulsars/lightcurves/xtej1859.html>

6.1.14. KS 1947+300

KS 1947+300 was first discovered with Mir-Kvant/TTM (Borozdin et al. 1990) and successively re-discovered with BATSE as the pulsating source GRO J1948+32 with a spin period of ~ 19 s (Chakrabarty et al. 1995). These were later identified as the same source, KS 1947+300 (Swank & Morgan 2000). The orbital period is 42 days, while the binary orbit is almost circular, $e \sim 0.03$ (Galloway et al. 2004). The Gaia measured distance is $15.2^{+3.7}_{-2.8}$ kpc, approximately consistent with the distance of ~ 10 kpc measured by Negueruela et al. (2003) and that of 10.4 ± 0.9 kpc measured by Riquelme et al. (2012), who also derived the stellar type (B0V) of the optical companion. KS 1947+300 is the only known BeXRB with an almost circular orbit that shows both Type I and II outbursts. During these outbursts, the source shows a spin-up trend, with a rate measured for the 2013 Type II outburst of $(2-4) \times 10^{-11} \text{ Hz s}^{-1}$ (Galloway et al. 2004; Ballhausen et al. 2016; Epili et al. 2016), while the source is spinning down between outbursts at an average rate of $-8 \times 10^{-13} \text{ Hz s}^{-1}$, as measured by GBM.²⁴

6.1.15. 2S 1417–624

Pulsations with a period of 17.6 s were discovered from 2S 1417–624 with SAS-3 observations in 1978 (Apparao et al. 1980; Kelley et al. 1981). This source shows both Type I and Type II outbursts, as well as decade-long quiescent periods. The orbital period is 42 days (Finger et al. 1996b), with the optical counterpart identified as a B-type (most likely a Be-type) star located at a distance of 1.4–11.1 kpc (Grindlay et al. 1984), while the measured Gaia distance²⁵ is $3.8^{+2.8}_{-1.8}$ kpc. The secular slow spin-down trend observed during quiescence is overshadowed by the large spin-up induced during its Type II outbursts, observed to be²⁶ $1.3 \times 10^{-12} \text{ Hz s}^{-1}$ (Raichur & Paul 2010a). Recently, 2S 1417–624 entered a new giant outburst episode at an orbital phase of ~ 0.30 , similar to the previous outburst in 2009 (Gupta et al. 2018; Nakajima et al. 2018; Ji et al. 2020).

6.1.16. SMC X-3

SMC X-3 was discovered with SAS-3 as a bright source in the Small Magellanic Cloud (Clark et al. 1978). However, it was not until 2004 that Chandra data analyzed by Edge et al. (2004) recognized this source as an ~ 8 s pulsar found by Corbet et al. (2004) with RXTE. The orbital period of the binary system is 45 days (Townsend et al. 2017), and the optical companion is a B1–1.5 IV–V star (McBride et al. 2008). In 2016, the source underwent a Type II outburst that reached a super-Eddington bolometric peak luminosity of $2.5 \times 10^{39} \text{ erg s}^{-1}$, making SMC X-3 a BeXRB system that is also a ULX source (Townsend et al. 2017). During that episode,²⁷ the NS spun-up at an outstanding rate of $6.8 \times 10^{-11} \text{ Hz s}^{-1}$ (Townsend et al. 2017). Conversely, the long-term (measured

from 1998 to 2012) spin-down trend has an average rate that is about 500 times slower, $-1.4 \times 10^{-12} \text{ Hz s}^{-1}$ (Klus et al. 2014).

6.1.17. EXO 2030+375

EXO 2030+375 is a transient source discovered with EXOSAT (Parmar et al. 1989). The NS spin period is 41.7 s, while the orbital period is ~ 46 days (Wilson et al. 2008). The orbit of the NS around the O9–B2 stellar companion is eccentric, $e = 0.4190$. Since its discovery, the source has shown both Type I and II outbursts. Type I episodes have been occurring nearly every orbit for ~ 28 yr with a typical duration of about 7–14 days, while Type II outbursts can last as long as 80 days. EXO 2030+375 is the XRP with the largest number of observed Type I outbursts (~ 150), detected in the X-ray band by many space-based observatories, e.g., Tenma, Ginga, ASCA, BATSE, RXTE, and more recently with Swift/BAT and GBM (Laplace et al. 2017). The long-term spin derivative trend observed by both BATSE and GBM²⁸ is spin-up at a mean rate of $\dot{\nu} \sim 1.3 \times 10^{-13} \text{ Hz s}^{-1}$. During such long-term spin-up periods, outbursts occur typically 5–6 days after periastron passage. However, the source has shown two torque reversals, one of which was ongoing in 2019. The first torque reversal occurred in 1995, which was first preceded by a ~ 3 yr quiescent period, accompanied later by a shift in the outburst peak to 8–9 days earlier than the preceding outbursts (3–4 days before periastron; Reig & Coe 1998; Wilson et al. 2002). Recently, the source has shown another quiescent period (~ 1 yr), after which the resumed activity was characterized by similar properties to those observed 20 yr before—a shift in the outburst peak orbital phase and a spin-down trend. This behavior highlights a possible 21 yr cycle due to Kozai–Lidov oscillations in the Be disk (Laplace et al. 2017). According to Laplace et al. (2017), the shift in the peak orbital phase is ~ 0.15 over the past cycle. To verify their predictions, we calculated the orbital shift of the outburst peak using the Swift/BAT monitor. To achieve this, we modeled each Type I outburst observed by the BAT with a skewed Gaussian profile, whose peak was taken to the corresponding outburst peak time. These are shown in Figure 2 as a function of time from 2016 January (MJD 57400) up to 2019 October (MJD 58700). At the time of writing, GBM recorded the start of a new spin-up phase, similar to what was observed in the previous cycle (Laplace et al. 2017). This supports the hypothesis formulated by those authors about a ~ 20 yr periodicity in the X-ray behavior of EXO 2030+375.

6.1.18. MXB 0656–072

Despite the discovery of MXB 0656–072 more than 40 yr ago with SAS-3 (Clark et al. 1975), it took almost 30 yr to detect any pulsations from this source with RXTE. RXTE observed the source to have a spin period of ~ 160 s (Morgan et al. 2003). The orbital period is about 100 days (Yan et al. 2012), and the optical companion is an O9.7 Ve star (Pakull et al. 2003; Nespoli et al. 2012). The Gaia measured distance is $5.1^{+1.4}_{-1.0}$ kpc, consistent with the distance derived from optical analysis of the companion spectrum (McBride et al. 2006). So far, the source has shown only Type I outbursts, with a peak luminosity of $< 10^{37} \text{ erg s}^{-1}$. The source has also shown

²⁴ <https://gammaray.msfc.nasa.gov/gbm/science/pulsars/lightcurves/ks1947.html>

²⁵ Recently, Ji et al. (2020) adopted a different Gaia counterpart to the source, which has a distance of $9.9^{+3.1}_{-2.4}$ kpc. This estimated distance is however inconsistent with the inferred distance of ~ 20 kpc calculated using accretion-driven torque models.

²⁶ <https://gammaray.msfc.nasa.gov/gbm/science/pulsars/lightcurves/2s1417.html>

²⁷ <https://gammaray.msfc.nasa.gov/gbm/science/pulsars/lightcurves/smcx3.html>

²⁸ <https://gammaray.msfc.nasa.gov/gbm/science/pulsars/lightcurves/exo2030.html>

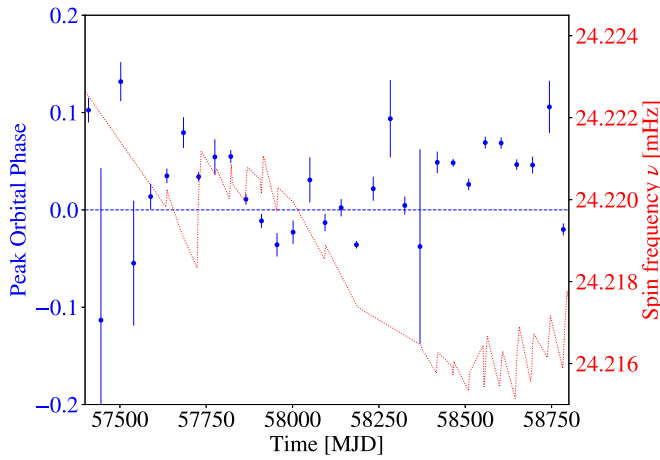


Figure 2. Blue y-axis: the evolution of the orbital phase shift of Type I outbursts from EXO 2030+375 as measured with Swift/BAT (blue dots). Recently, the outbursts peak at ~ 0.1 in orbital phase, a behavior that seems to be recurring with a periodicity of ~ 20 yr (see the text). Red y-axis: the evolution of the NS spin frequency (corrected for the orbital motion) as measured with GBM (red dashed line). The pulsar is now entering a new spin-up phase, after about 2000 days of spin-down, similar to what observed ~ 20 yr ago.

fast spin-up during accretion. A spin-up trend of $\dot{\nu} \sim 5 \times 10^{-12} \text{ Hz s}^{-1}$ (that is about 0.45 s in 30 days) was observed in the 2003 outburst (McBride et al. 2006). The last series of Type I outbursts observed from this source dates back to the period between 2007 and 2009 (Yan et al. 2012); afterwards, the source entered a quiescent period that is still presently ongoing. The spin-up rate measured by GBM²⁹ during the last of those outbursts was comparable to that measured in 2003.

6.1.19. GS 0834–430

Pulsations from GS 0834–430 were first observed with Ginga, each lasting 12 s (Aoki et al. 1992). The orbital period was measured to be 106 days by Wilson et al. (1997). This was determined by using the spacing between the first five of seven outbursts observed between 1991 and 1993, while the last two were spaced by about 140 days. The optical counterpart is a B0–2 III–Ve type star and estimated to be located at a distance of 3–5 kpc, inferred from the luminosity type (Israel et al. 2000). This was later found to be consistent with the measured Gaia distance of $5.5^{+2.5}_{-1.7}$ kpc for the closest counterpart located at $5''.4$ from the nominal source position.

The average spin-up rate during the first outbursting period was about $6 \times 10^{-12} \text{ Hz s}^{-1}$ (Wilson et al. 1997), while the spin-up rate measured by GBM³⁰ during the last outburst in 2012 was found to be $1.1 \times 10^{-11} \text{ Hz s}^{-1}$ (Jenke et al. 2012a).

6.1.20. GRO J2058+42

Pulsations from this source were discovered by BATSE to have a spin period of 198 s during a giant X-ray outburst in 1996 (Wilson et al. 1996). Subsequent observations of the source found an orbital period of about 110 days (Wilson et al. 1998) and were consequently identified later as a BeXRB system (Wilson et al. 2005). The first estimation of the distance

to the source (Wilson et al. 1998) was found to be 7–16 kpc away, consistent with the GAIA distance of $8.0^{+1.2}_{-1.0}$ kpc. During the giant outburst in 1996, the source showed spin-up at a rate of $1.7 \times 10^{-11} \text{ Hz s}^{-1}$ (Wilson et al. 1998). GRO J2058+42 was observed by GBM³¹ only during the recent bright X-ray outburst (Malacaria et al. 2019), when the source showed a spin-up rate similar to that reported in 1996. It was previously unobserved by GBM, thus, representing the most recent addition to the GBM Pulsar catalog.

6.1.21. A 0535+26

Pulsations from A 0535+26 were discovered by Ariel 5 with a period of 103 s (Coe et al. 1975; Rosenberg et al. 1975). The system has an orbital period of 111 days (Nagase et al. 1982). The optical counterpart is HD 245770, an O9.7–B0 IIIe star located at a distance of ~ 2 kpc (Hutchings et al. 1978; Li et al. 1979; Giangrande et al. 1980; Steele et al. 1998). This distance was later confirmed by Gaia to be $2.1^{+0.3}_{-0.2}$ kpc. The system regularly shows Type I outbursts, separated by both quiescent phases and Type II episodes (see Motch et al. 1991; Müller et al. 2013 and references therein). Similar to GX 1+4 and GRO J1008–57 (see Sections 6.2.8 and 6.1.27, respectively), little to no spin-up is detected during Type I outbursts of this source. However, large spin-up trends have been observed during Type II outbursts. The source is found to be spinning down during quiescence.³² The average spin-down rate is $1.4 \times 10^{-11} \text{ Hz s}^{-1}$ (see, e.g., Hill et al. 2007), while the measured spin-up rate during the giant outburst episodes is $\sim (6\text{--}12) \times 10^{-12} \text{ Hz s}^{-1}$ (Camero-Arranz et al. 2012; Sartore et al. 2015).

6.1.22. IGR J19294+1816

IGR J19294+1816 was initially discovered with International Gamma-Ray Astrophysics Laboratory (INTEGRAL; Turler et al. 2009) and later recognized as a pulsating source by Swift (Rodríguez et al. 2009a, 2009b), with a pulsation period of ~ 12 s. An orbital period of 117 days has been proposed, although this remains uncertain (Corbet et al. 2009; Rodríguez et al. 2009b; Bozzo et al. 2011). The Gaia measured distance is $2.9^{+2.5}_{-1.5}$ kpc. However, independent measurements of the distance report inconsistent values. A lower limit has been estimated to be >8 kpc for a B3 I optical counterpart by Rodríguez et al. (2009a), while a distance of 11 kpc was inferred by Rodes-Roca et al. (2018) for a B1 Ve counterpart. Inspection of the GBM data³³ reveals a secular spin-down trend with $\dot{\nu} \sim -2 \times 10^{-12} \text{ Hz s}^{-1}$, interrupted by local spin-up episodes accompanying accretion during outbursts, with an average spin-up of about $\dot{\nu} \sim 2.5 \times 10^{-11} \text{ Hz s}^{-1}$. GBM observations support the ~ 117 days periodicity. According to the most recent observations by GBM and XMM (Domček et al. 2019), the source still exhibits a long-term spin-down trend, with Type I outbursts at each periastron passage.

6.1.23. GX 304-1

Pulsations with a period of ~ 272 s from GX 304-1 were discovered with SAS-3 in 1978 (McClintock et al. 1977b). The

²⁹ <https://gammaray.msfc.nasa.gov/gbm/science/pulsars/lightcurves/mxb0656.html>

³⁰ <https://gammaray.msfc.nasa.gov/gbm/science/pulsars/lightcurves/gs0834.html>

³¹ <https://gammaray.msfc.nasa.gov/gbm/science/pulsars/lightcurves/groj2058.html>

³² <https://gammaray.msfc.nasa.gov/gbm/science/pulsars/lightcurves/a0535.html>

³³ <https://gammaray.msfc.nasa.gov/gbm/science/pulsars/lightcurves/igrj19294.html>

orbital period is about 132 days, and the optical companion has been identified as a B2 Vne type star. The distance measured by GAIA to the companion was found to be $2.01^{+0.15}_{-0.13}$ kpc, in agreement with a previously measured distance of 2.5 kpc (Mason et al. 1978; Parkes et al. 1980). The source typically shows both Type I and II outbursts, as well as long (\sim yr) quiescent periods. According to GBM observations,³⁴ the source shows accretion-driven spin-up episodes at a rate of about $\dot{\nu} \sim 1 \times 10^{-12} \text{ Hz s}^{-1}$ during active periods and long-term spin-up trends at an average rate of about $\dot{\nu} \sim 1.3 \times 10^{-13} \text{ Hz s}^{-1}$. A spin-down rate between outbursts of $\dot{\nu} \sim -5 \times 10^{-14} \text{ Hz s}^{-1}$ (Malacaria et al. 2015; Sugizaki et al. 2015) has also been observed in the data. Recently, the source has entered a new period of quiescence, probably due to major disruptions of the Be disk following a Type II outburst, showing only sporadic X-ray activity (Malacaria et al. 2017).

6.1.24. RX J0440.9+4431

Pulsations with a period of 202 s from RX J0440.9+4431 were discovered with RXTE (Reig & Roche 1999). The binary orbital period is 150 days (Ferrigno et al. 2013 and references therein), and the optical companion is a B0.2 Ve star with a Gaia measured distance of $3.2^{+0.7}_{-0.5}$ kpc, consistent with previous measurements of \sim 3.3 kpc (Reig et al. 2005). Only Type I outbursts have been observed from this source, the first and brightest of which was detected in 2010 (Usui et al. 2012), exhibiting a spin-up rate of about $\dot{\nu} \sim 4.5 \times 10^{-12} \text{ Hz s}^{-1}$ in GBM.³⁵ A strong, long-term spin-down trend has also been observed between the first pulsations discovered from the source in 1999 (\approx 206 s) and the outburst analyzed 12 yr later. Pulsation periods from the latter were measured at \approx 202 s, resulting in a spin-down rate of about $\dot{\nu} = -3 \times 10^{-12} \text{ Hz s}^{-1}$ (Ferrigno et al. 2013).

6.1.25. XTE J1946+274

Pulsations with a period of \sim 15 s were first detected from XTE J1946+274 by RXTE (Smith et al. 1998). The orbital period is about 169 days (Wilson et al. 2003), and the optical companion is a B0-1 IV-Ve star with a measured Gaia distance of $12.6^{+3.9}_{-2.9}$ kpc, consistent with previous measurements of 8–10 kpc (Verrecchia et al. 2002; Wilson et al. 2003; Riquelme et al. 2012). A number of Type I and II outbursts have been observed from this source, as well as long quiescent periods.³⁶ During accretion, the source shows strong spin-up at an average rate of $\dot{\nu} \sim (5\text{--}10) \times 10^{-12} \text{ Hz s}^{-1}$ (Wilson et al. 2003; Doroshenko et al. 2017). During quiescent periods, the source spins-down with a rate of about $\dot{\nu} = -2.3 \times 10^{-13} \text{ Hz s}^{-1}$ over a long-term trend. Recently, the source has shown another bright outburst episode, monitored with GBM and NICER (Jenke et al. 2018a). Analysis of these data is ongoing (B. Mailyan et al. 2020, in preparation).

6.1.26. 2S 1845–024

Pulsations from 2S 1845–024 (GS 1843–024) were discovered with Ginga with a spin period of \sim 30 s (Makino

& GINGA Team 1988a). The orbital period is about 242 days (Zhang et al. 1996; Finger et al. 1999). No optical counterpart is currently known for this system. However, based on the Corbet diagram and the regularity of the observed outbursts, this source has been identified as a BeXRB. No Gaia measurement of the distance is available for this source in the DR2, but an inferred distance of \sim 10 kpc has been obtained from the analysis of the X-ray spectral properties of the source (Koyama et al. 1990). No Type II outbursts have been observed from this source. A secular spin-up trend has been measured with BATSE during the first \sim 5.5 yr after its discovery. It results from fast local spin-up occurring during outburst episodes. This was found to occur at a rate of $\dot{\nu} \sim 4 \times 10^{-12} \text{ Hz s}^{-1}$, which yielded a long-term spin-up trend with a rate of $\dot{\nu} \sim 2.7 \times 10^{-13} \text{ Hz s}^{-1}$ (Finger et al. 1999). More recently, the source has inverted its long-term trend and has now been in a spin-down phase for around 10 yr.³⁷ The strength of the local spin-up episodes associated with outbursting episodes ($\dot{\nu} \sim 3.5 \times 10^{-12} \text{ Hz s}^{-1}$), as well as that of the long-term spin-down trends ($\dot{\nu} \sim -2.4 \times 10^{-13} \text{ Hz s}^{-1}$), is similar to the strength of those preceding the torque reversal. A comprehensive spin history for this source is shown in Figure 3. An estimation of the torque reversal time can be inferred assuming that the long-term linear trends seen separately for BATSE data up to 51560 MJD and after 56154 MJD for GBM data can be extrapolated to periods where neither BATSE nor GBM data were available. This returns a torque reversal time of 53053 ± 250 MJD, where the uncertainty is derived by extrapolating the two separate linear fits within the uncertainty of their parameters.

6.1.27. GRO J1008–57

Pulsations from GRO J1008–57 were discovered by CGRO during an X-ray outburst in 1993 (Stollberg et al. 1993). The NS has a spin period of about 93.5 s, while the binary orbital period is \sim 248 days (Levine & Corbet 2006; Coe et al. 2007; Kühnel et al. 2013). The optical counterpart is either a dwarf (luminosity class III) or a supergiant (V) O9e-B1e type star (Coe et al. 1994a). There is no available Gaia distance for this source, but Riquelme et al. (2012) estimates the system to be at a distance of either 9.7 or 5.8 kpc, according to the luminosity type of the companion star. As with GX 1+4 (see Section 6.2.8) and A0535+26 (see Section 6.1.21), the source exhibits a secular spin-down trend interrupted by brief spin-up episodes correlated with bright flux levels, typical of Type II outbursts.³⁸ The spin-up rate observed during the 2012 giant outburst is $6 \times 10^{-12} \text{ Hz s}^{-1}$, while the secular spin-down rate is about $-2.3 \times 10^{-14} \text{ Hz s}^{-1}$, induced by the propeller accretion mechanism in that regime (Kühnel et al. 2013). The source typically undergoes an outburst at each periastron passage, with recent activity characterized by peculiar outburst light curves with 2–3 peaks and a peak luminosity of several times $10^{37} \text{ erg s}^{-1}$ (Nakajima et al. 2014; Kühnel et al. 2017). Applying the orbital solution found for this source by Kuehnel et al. (2014) still shows orbital signatures in GBM data, and we therefore do not consider its pulse frequency history as demodulated.

³⁴ <https://gammaray.msfc.nasa.gov/gbm/science/pulsars/lightcurves/gx304m1.html>

³⁵ <https://gammaray.msfc.nasa.gov/gbm/science/pulsars/lightcurves/rxj0440.html>

³⁶ <https://gammaray.msfc.nasa.gov/gbm/science/pulsars/lightcurves/xtej1946.html>

³⁷ <https://gammaray.nsstc.nasa.gov/gbm/science/pulsars/lightcurves/2s1845.html>

³⁸ <https://gammaray.msfc.nasa.gov/gbm/science/pulsars/lightcurves/groj1008.html>

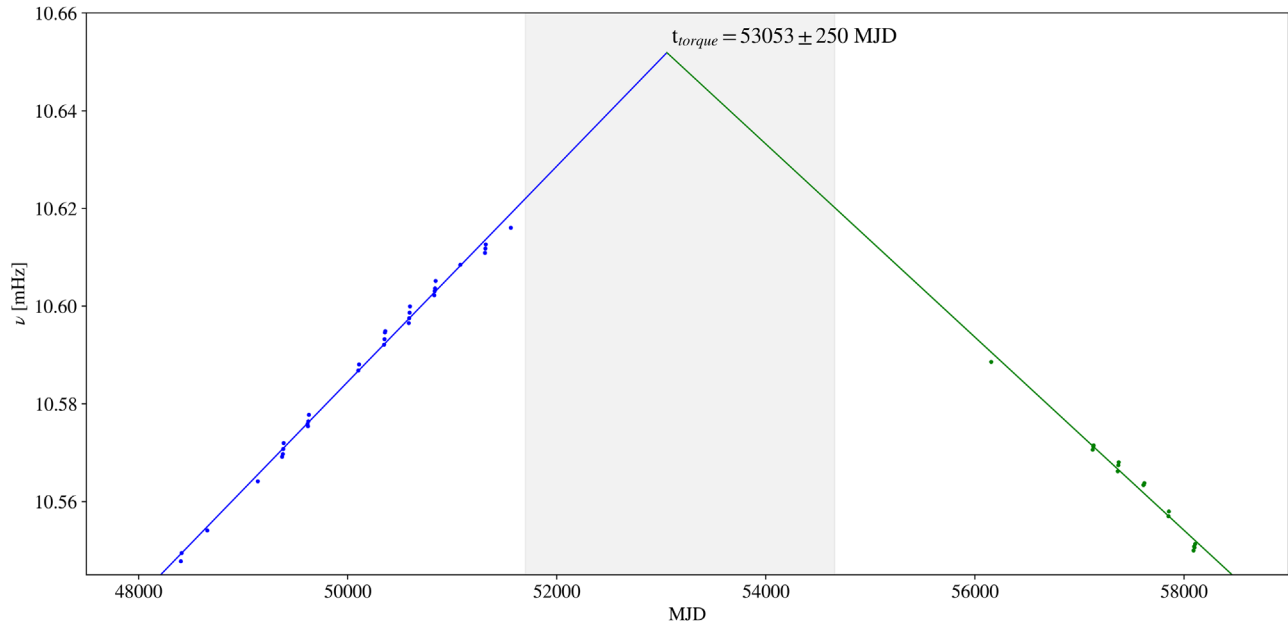


Figure 3. Spin history of the BeXRB 2S 1845–024 as observed by BATSE (blue) and GBM (green). Errors are smaller than data points. Two separated linear fits are shown as straight lines for the BATSE (blue) and GBM (green) data. The estimated torque time is inferred from the intersection of the linear fit lines, 53053 ± 250 MJD (see Section 6.1.26). The gray shaded area marks the period where neither BATSE nor GBM data are available.

6.1.28. Cep X-4

Pulsations from Cep X-4 at ~ 66 s were first detected with Ginga (Makino & GINGA Team 1988b). Only a handful of outbursts with a relatively low luminosity have been observed from this source; thus, the orbital elements for this binary system are still unknown. However, a possible orbital period of about 21 days has been suggested by Wilson et al. (1999) and McBride et al. (2007). The optical counterpart has been identified as a possible B1-2 Ve star (Bonnet-Bidaud & Mouchet 1998). The same authors have tentatively estimated a distance to the source of about 4 kpc, but this value has been challenged by Riquelme et al. (2012) who proposed a distance of either 7.9 or 5.9 kpc according to whether the stellar type of the companion is a B1 or B2 star, respectively. The distance of 4 kpc also does not agree with the measured Gaia distance of $10.2^{+2.2}_{-1.6}$ kpc. Between 1993 and 1997, Wilson et al. (1999) used BATSE data to measure an average spin-down rate of $\dot{\nu} \sim -4 \times 10^{-14} \text{ Hz s}^{-1}$. Spin-up has also been observed during accretion episodes at a rate of $\sim 10^{-12} \text{ Hz s}^{-1}$. At the time of writing, the source is still showing a general spin-down trend.³⁹

6.1.29. IGR J18179–1621

Pulsations from IGR J18179–1621 were discovered by Swift with a spin period of about 12 s (Halpern 2012). This was later confirmed by Fermi/GBM (Finger & Wilson-Hodge 2012) detections of its pulsations.⁴⁰ The only activity reported from this source is the same that led to its discovery in 2012, when the source slightly brightened and became detectable by INTEGRAL and other X-ray satellites (see Bozzo et al. 2012 and references therein). The nature of the optical companion is uncertain, but the analysis of the spectral characteristics of the source along with the presence of pulsations suggest that it

belongs to the class of HMXBs/BeXRBs (Nowak et al. 2012; Tuerler et al. 2012). There is no measured Gaia distance for this source in the DR2, but a value of $8.0^{+2.0}_{-7.0}$ kpc was found by Nowak et al. (2012).

6.1.30. MAXI J1409–619

Pulsations from MAXI J1409–619 were discovered by Swift, with an NS spin period of about 500 s (Kennea et al. 2010) and later confirmed by GBM (Camero-Arranz et al. 2010b), which also detected a spin-up during a follow-up observation, as the source re-brightened a few weeks after its discovery. In the GBM data,⁴¹ the frequency increased at a rate of $1.6 \times 10^{-11} \text{ Hz s}^{-1}$ during the outburst observed in 2010 December. Only a handful of observations have been carried out for this source immediately following its discovery. Consequently, very little is known about it. Given the shape of its light curve, the characteristics of its X-ray spectrum, its location close to the Galactic plane, and its vicinity of an infrared counterpart (2MASS 14080271–6159020), MAXI J1409–619 has been suggested to be an SFXE candidate (Kennea et al. 2010). There is no Gaia counterpart consistent with the X-ray source position as measured by Swift/XRT, but the distance to this source has been measured by Orlandini et al. (2012) as 14.5 kpc. After the last GBM observation in 2010 December, the source has remained in a state of quiescence.

6.1.31. XTE J1858+034

Pulsations at a spin period of about 221 s from XTE J1858+034 were discovered by RXTE (Remillard et al. 1998; Takeshima et al. 1998). The source was discovered during one of only a few recorded outburst episodes (see also Molkov et al. 2004), the last one being recorded by GBM in 2010⁴²

³⁹ <https://gammaray.msfc.nasa.gov/gbm/science/pulsars/lightcurves/cepx4.html>

⁴⁰ <https://gammaray.msfc.nasa.gov/gbm/science/pulsars/lightcurves/igrj18179.html>

⁴¹ <https://gammaray.msfc.nasa.gov/gbm/science/pulsars/lightcurves/maxij1409.html>

⁴² <https://gammaray.msfc.nasa.gov/gbm/science/pulsars/lightcurves/xtej1858.html>

(Krimm et al. 2010). The orbital period of the binary is currently unknown, and the spectral type of the companion is still uncertain, but there are indications that it is a Be-type star (Reig et al. 2004a, 2005). The closest counterpart measured by Gaia is located at an angular offset $3''.5$ from the nominal source position, at a distance of $1.55^{+0.28}_{-0.21}$ kpc. There are no other available counterparts for this source. The spin-up measured by GBM (uncorrected for binary modulation) during the 2010 accretion episode is about $1 \times 10^{-11} \text{ Hz s}^{-1}$.

6.2. Persistent Binary Systems

6.2.1. 4U 1626–67

4U 1626–67 is an LMXB discovered by Uhuru in 1977 (Giacconi et al. 1972). The NS spins with a period of 7.66 s while orbiting its companion star, *KZ TrA*, in only 42 minutes (Middleditch et al. 1981; Chakrabarty 1998). The optical companion is a very low-mass star ($<0.1 M_{\odot}$; McClintock et al. 1977a, 1980). The Gaia measured distance to the star is $3.5^{+2.3}_{-1.3}$ kpc, consistent with more recent measurements of $3.5^{+0.2}_{-0.3}$ kpc by Schulz et al. (2019). Since its discovery, the source has shown two major torque reversal episodes. The first was estimated to happen in 1990 (Wilson et al. 1993; Bildsten et al. 1994) when the source switched from a steady spin-up trend, with a rate of $\dot{\nu} = 8.5 \times 10^{-13} \text{ Hz s}^{-1}$ that was observed for over a decade, to a ~ 7 yr long steady spin-down trend, with a rate of $\dot{\nu} = -3.5 \times 10^{-13} \text{ Hz s}^{-1}$ (Chakrabarty et al. 1997). The second torque reversal episode was observed by GBM⁴³ and Swift/BAT in 2008, when the source started a new spin-up trend. As of 2019 November, the source is still spinning up, with a mean rate of $\dot{\nu} = 4 \times 10^{-13} \text{ Hz s}^{-1}$ (Camero-Arranz et al. 2010a).

6.2.2. Her X-1

Her X-1 was discovered by Uhuru in 1971 (Tananbaum et al. 1972). It is an eclipsing LMXB and one of the most studied accreting X-ray pulsars. The NS spin period is about 1.2 s, while the orbital period is ~ 1.7 days. The optical companion is an A7-type star (Reynolds et al. 1997), with a Gaia measured distance of $5.0^{+0.8}_{-0.6}$ kpc, consistent with previous measurements of $6.1^{+0.9}_{-0.4}$ kpc (Leahy & Abdallah 2014). The system exhibits super-orbital X-ray modulation with a period of ~ 35 days, most likely driven by a precessing warped accretion disk (see Scott et al. 2000; Leahy & Igna 2010; Kotze & Charles 2012 and references therein) or by a precessing NS (Postnov et al. 2013). The general trend of the pulse period evolution is that of spin-up at an average rate of $\dot{\nu} = 5 \times 10^{-13} \text{ Hz s}^{-1}$ (see, e.g., Klochkov et al. 2009). It occasionally exhibits spin-down episodes of a moderately larger entity, $\dot{\nu} = -7 \times 10^{-12} \text{ Hz s}^{-1}$ (Bildsten et al. 1997). Recently, GBM measurements⁴⁴ have shown that the spin derivative trend has flattened around a spin frequency of 807.937 mHz.

6.2.3. Cen X-3

The bright, persistent source, Cen X-3, was discovered by the Uhuru satellite in 1971 and marks the first observation of this accreting X-ray pulsar (Giacconi et al. 1971). The NS spin

period is about 4.8 s, and the orbital period of the NS is ~ 2.1 days (Kelley et al. 1983b; Falanga et al. 2015) in an almost circular orbit ($e < 0.0016$) around V779 Cen, an O6-7 supergiant companion star (Krzeminski 1974; Hutchings et al. 1979; Ash et al. 1999). The Gaia measured distance is $6.4^{+1.4}_{-1.1}$ kpc, consistent with previous measurements of 5.7 ± 1.5 kpc (Thompson & Rothschild 2009). Optical observations first revealed the presence of an accretion disk around the pulsar (Tjemkes et al. 1986). X-ray monitoring of the source later on found that the secular trend of the NS frequency is to spin-up; although, long spin-down periods have also been observed (Nagase 1989b). GBM observations show that typical spin-up rates are of the order of $\dot{\nu} = 3 \times 10^{-12} \text{ Hz s}^{-1}$. Although the NS is accreting from a disk, there appears to be no correlation between the spin derivative and the observed X-ray flux in Cen X-3 (Tsunemi et al. 1996; Raichur & Paul 2008a, 2008b). Instead, the high, aperiodic source variability is likely due to a radiatively warped accretion disk (Iping & Petterson 1990) that does not reflect a real modulation of the accretion rate. The most likely scenario is that the mass transfer in this system is dominated by RLO with wind-accretion (and wind-captured disk) contributions (Walter et al. 2015; El Mellah et al. 2019 and references therein). Orbital decay has also been observed for this source, at an average rate of $\dot{P}_{\text{orb}}/P_{\text{orb}} = -1.800(1) \times 10^{-6} \text{ yr}^{-1}$ and interpreted in terms of tidal interaction plus rapid mass transfer between the NS and its massive companion (Nagase et al. 1992; Falanga et al. 2015). The long-term spin derivative is likely due to an accretion disk moving with alternating rotational direction, with a proposed periodicity in the Ginga data of about 9 yr (Tsunemi et al. 1996). However, the combined BATSE and GBM⁴⁵ spin frequency and pulsed flux history for this source reveal a more complex behavior and show alternating long-term spin-down and spin-up trends with random-walk variations superimposed (de Kool & Anzer 1993).

6.2.4. 4U 1538–52

Pulsations from 4U 1538–52 were first discovered in 1976 by the Ariel 5 mission, which revealed a spin period of 530 s (Davison et al. 1977). The NS is in a 3.7 day, slightly eccentric ($e \sim 0.2$) orbit (Davison et al. 1977; Corbet et al. 1993; Clark 2000). The supergiant companion is a B0e-type star, called QV Nor (Parkes et al. 1978). The Gaia measured distance is $6.6^{+2.2}_{-1.5}$ kpc, consistent with a previous measurement of $5.8^{+2.0}_{-1.9}$ kpc by Güver et al. (2010). Early observations of this source show a long-term spin-down trend with random short-term variations (Makishima et al. 1987; Nagase 1989a), while later observations find a reverse of the general long-term trend, probably happening in 1988. The average spin-up rate of $\dot{\nu} = 1.8 \times 10^{-14} \text{ Hz s}^{-1}$ is of the same order of magnitude as the previous spin-down period (Rubin et al. 1997). This spin-up period went on at least until 2006 (Baykal et al. 2006). As of 2019 November, GBM⁴⁶ has been observing the source in a new spin-down trend since the beginning of its operations in 2008. The binary source also shows hints of orbital decay, $\dot{P}_{\text{orb}}/P_{\text{orb}} = (0.4 \pm 1.8) \times 10^{-6} \text{ yr}^{-1}$ (Baykal et al. 2006),

⁴³ <https://gammaray.msfc.nasa.gov/gbm/science/pulsars/lightcurves/4u1626.html>

⁴⁴ <https://gammaray.msfc.nasa.gov/gbm/science/pulsars/lightcurves/herx1.html>

⁴⁵ <https://gammaray.msfc.nasa.gov/gbm/science/pulsars/lightcurves/cenx3.html>

⁴⁶ <https://gammaray.msfc.nasa.gov/gbm/science/pulsars/lightcurves/4u1538.html>

similar to the value observed in other X-ray binaries, yet consistent with a null value.

6.2.5. Vela X-1

X-ray pulsations from Vela X-1 were discovered by the SAS-3 satellite in 1975 (McClintock et al. 1977a), revealing a spin period of about 283 s. The X-ray source is eclipsing, with an orbital period of ~ 8.9 days (Falanga et al. 2015 and references therein). The orbit is almost circular ($e \sim 0.09$) around HD77581, a B0.5Ia, supergiant (Brucato & Kristian 1972; Hiltner et al. 1972; van Kerkwijk et al. 1995). The Gaia measured distance of $2.42^{+0.19}_{-0.17}$ kpc is consistent with previous measurements of 2.0 ± 0.2 kpc (Giménez-García et al. 2016 and references therein). The ellipsoidal variation of the optical light curve of the stellar companion suggests the star is distorted due to the tidal forces from the NS (Koenigsberger et al. 2012 and references therein). The NS is believed to be wind-fed as the evolution of the spin frequency does not show any steady long-term trend, but is instead observed to take a random-walk path (Deeter et al. 1989; de Kool & Anzer 1993). However, the geometrical configuration of the binary system is such that a more complex phenomenology needs to be taken into account. Both simulated and observational studies (see, e.g., Blondin et al. 1991; Kaper et al. 1994; Sidoli et al. 2015; Malacaria et al. 2016) have shown that three different structures are present in the binary: a photoionization wake due to the Strömgren sphere around the NS, a tidal stream due to the almost filled Roche lobe of the donor, and a turbulent accretion wake in which transient accretion disks with alternating directions of rotation form around the NS (see also Fryxell & Taam 1988; Blondin & Raymer 2012). Recent works also show that wind-captured transient disks can form in the ambient wind of Vela X-1 (see, e.g., El Mellah et al. 2019). Those transient accretion disks are thought to be responsible for the sparse spin-up/spin-down episodes observed by GBM at random epochs.⁴⁷ The spin-up rate observed during such episodes is of the order of $\dot{\nu} = 1 - 2 \times 10^{-13} \text{ Hz s}^{-1}$, with milder rates for spin-down episodes, $\dot{\nu} = -2 \times 10^{-14} \text{ Hz s}^{-1}$. With a magnetic field of $2.6 \times 10^{12} \text{ G}$ (Fürst et al. 2014 and references therein) and an average luminosity of $5 \times 10^{36} \text{ erg s}^{-1}$, and using $\Pi_{\text{su}} = 8$ from Shakura et al. (2014), the quasi-spherical settling accretion model (Equation (13)) predicts a spin-up value of $\dot{\nu} = 3 \times 10^{-14} \text{ Hz s}^{-1}$, a factor of ~ 4 weaker than what was actually observed. On the other hand, the spin-up rate expected by accretion-disk theory (see Equation (21)) is $\sim 1.4 \times 10^{-12} \text{ Hz s}^{-1}$, almost an order of magnitude faster than the observed one. Up to now, no clear correlation has been reported between the observed spin derivative episodes and the X-ray luminosity for this source.

6.2.6. OAO 1657–415

Pulsations from OAO 1657–415 were discovered by HEAO-1 with a spin period of about 38 s (White & Pravdo 1979). The orbital period is 10.4 days, with an eclipse occurring for 1.7 days (Chakrabarty et al. 1993). Accretion onto the NS is fed by an optical companion that is currently believed to be in a transitional stage between an OB and Wolf–Rayet star, of the spectral type Ofpe/WN9 (Mason et al. 2009). The closest counterpart measured by Gaia is located at an angular offset of $4''.7$ from the

nominal source position, at a distance of $2.2^{+0.7}_{-0.5}$ kpc. However, previous measurements locate the system at a distance of about 4.4–12 kpc (Chakrabarty et al. 2002; Mason et al. 2009), consistent with the measurement of 7.1 ± 1.3 kpc by Audley et al. (2006). The pulsar exhibits a secular spin-up trend at an average rate of $\dot{\nu} \sim 8.5 \times 10^{-13} \text{ Hz s}^{-1}$, superimposed with several spin-up/spin-down episodes throughout its long history of observation. Analysis using BATSE and GBM⁴⁸ data allowed Jenke et al. (2012b) to establish two different modes of accretion: one resulting from transient, disk-driven accretion that leads to steady spin-up periods correlated with flux (see also Baykal 1997), while the other results from wind-driven accretion, in which the NS spins-down at a (slower) rate that is uncorrelated with flux. Recently, a “magnetic levitating disk” scenario has been proposed to explain the spin evolution in OAO 1657–415 (Kim & Ikhsanov 2017).

6.2.7. GX 301-2

GX 301-2 pulsations at ~ 680 s were discovered by Ariel 5 in 1976 (White et al. 1976). The NS is in an eccentric ($e \sim 0.5$), 41.5 day orbit (Sato et al. 1986) around Wray 77, a hypergiant, B1 Ia+ star (Vidal 1973; Parkes et al. 1980; Kaper et al. 1995). The measured Gaia distance is $3.1^{+0.6}_{-0.5}$ kpc, consistent with a previously estimated distance of 3.1 kpc (Hammerschlag-Hensberge et al. 1979; Kaper et al. 2006). GX 301-2 is a near-equilibrium rotator; thus, its net spin derivative is equal to zero. The secular spin period evolution is generally smooth and consistent with a random-walk evolution (de Kool & Anzer 1993). However, the source has shown rapid ($\dot{\nu} = (3-5) \times 10^{-12} \text{ Hz s}^{-1}$) and prolonged (~ 30 days) spin-up episodes (Koh et al. 1997), probably indicating the formation of a transient accretion disk.

Recently, GBM⁴⁹ observed another similar episode over a longer period (~ 40 days), which was also stronger ($\dot{\nu} \approx 6 \times 10^{-12} \text{ Hz s}^{-1}$) than was previously observed (Nabizadeh et al. 2019; Abarr et al. 2020; Malacaria et al. 2020, in preparation), during which NuSTAR measured an unabsorbed luminosity of $\sim 1.5 \times 10^{37} \text{ erg s}^{-1}$ at a corresponding spin-up rate of $\dot{\nu} \approx 3.6 \times 10^{-13} \text{ Hz s}^{-1}$ as measured by GBM around the NuSTAR observation. This is a factor of three lower than the spin-up rate predicted by Equation (13) of $\sim 1.1 \times 10^{-12} \text{ Hz s}^{-1}$. On the other hand, the spin-up rate predicted by the accretion-disk theory (see Equation (21)), assuming a magnetic field of $4 \times 10^{12} \text{ G}$ (Kreykenbohm et al. 2004), is $\sim 4 \times 10^{-12} \text{ Hz s}^{-1}$, about an order of magnitude stronger than the observed rate, but in agreement with the rate observed during the initial phase of the spin-up episode.

6.2.8. GX 1+4

GX 1+4 is an LMXB discovered by a balloon X-ray observation in 1970 (Lewin et al. 1971), with an NS spin period of ~ 2 minutes (Lewin et al. 1971). The orbital period is not yet well known. Old studies have reported periodic signals every 304 days in the optical band (e.g., Cutler et al. 1986) or at 1161 days in the X-ray band (e.g., Hinkle et al. 2006). However, RXTE data from GX 1+4 does not show modulation at any of these proposed periods (Corbet et al. 2008). The

⁴⁷ <https://gammaray.msfc.nasa.gov/gbm/science/pulsars/lightcurves/velax1.html>

⁴⁸ <https://gammaray.msfc.nasa.gov/gbm/science/pulsars/lightcurves/oa1657.html>

⁴⁹ <https://gammaray.msfc.nasa.gov/gbm/science/pulsars/lightcurves/gx301m2.html>

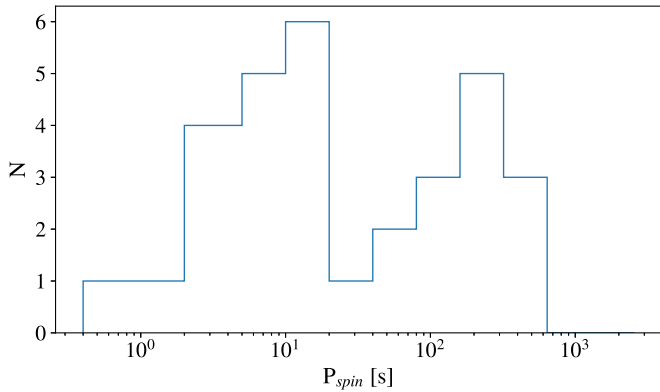


Figure 4. Spin period distribution of all GBM detected BeXRBs in the Milky Way.

donor companion is *V2116 Oph.* (Glass & Feast 1973), a type M6III red-giant star that under-fills its Roche-Lobe (Chakrabarty & Roche 1997; Hinkle et al. 2006). Therefore, it is assumed that the NS is wind-fed by the companion, making it part of the so-called symbiotic X-ray Binaries (SyXBs; Corbet et al. 2008; Yungelson et al. 2019). Different attempts have been made to determine the distance to the source (see, e.g., González-Galán et al. 2012 and references therein), but it still remains poorly constrained. The Gaia measured distance to the source is $7.5^{+4.3}_{-2.8}$ kpc. Ten years following its discovery, the source was spinning up strongly at an average rate of $\dot{\nu} = 6.0 \times 10^{-12} \text{ Hz s}^{-1}$ (Doty et al. 1981; Warwick et al. 1981; White et al. 1983). No observations were recorded from 1980 and 1983, as EXOSAT did not detect the source, indicating that the flux had decreased below the sensitivity of the instrument. The source reappeared in 1987 in observations by Ginga with a lower luminosity and exhibiting a torque reversal with an average spin-down rate of $\dot{\nu} = -3.7 \times 10^{-12} \text{ Hz s}^{-1}$ (Makishima et al. 1988; Nagase 1989a). With a magnetic field of $3.7 \times 10^{12} \text{ G}$ (Ferrigno et al. 2007), and assuming an average luminosity of $4 \times 10^{36} \text{ erg s}^{-1}$ (see González-Galán et al. 2012 and references therein), the quasi-spherical settling accretion model (Equation (12)) predicts a comparable spin-down value, $\dot{\nu} = -1.5 \times 10^{-12} \text{ Hz s}^{-1}$. GBM⁵⁰ observations show the source to still be undergoing a general spin-down trend, with occasional brief spin-up episodes corresponding to bright flux levels.

7. Discussion

The (almost) all-sky, continuous, long-term coverage of GBM provides fresh data that helps improve the analysis of accreting X-ray pulsars, providing enough statistics for interesting population studies. Examples of this are shown in Figures 4 and 5.

7.1. Bimodal Spin Period Distribution

Knigge et al. (2011) showed that the P_s – P_{orb} distribution in BeXRBs is bimodal. While the bimodality of P_{orb} is only marginal, the distribution of P_s has a clear gap at around 40 s and two distinct distributions peaking at ~ 10 s and ~ 200 s, respectively. Those authors proposed that the two distinct subpopulations are created by the type of supernovae that was

the progenitor for the formation of the NS. One is an electron-capture supernovae, which would produce NSs with shorter spin periods on average, while iron core-collapse supernovae would produce NSs with longer spin periods. Other explanations of the bimodality have also been described in previous studies. Cheng et al. (2014) proposed that the bimodal distribution is the result of two different accretion modes: (1) advection-dominated accretion flow (ADAF) disks, which are more likely to form during a Type I outburst, or (2) thin accretion disks formed during Type II outbursts. The ADAF disk is inefficient to spin-up the NS; thus, BeXRBs experiencing more Type I outbursts will produce NSs with longer spin periods. The thin disks produced as a result of Type II outbursts are more efficient in transferring angular momentum, and thus, BeXRBs dominated by this mechanism will spin-up the NS to the shorter spin period subpopulation.

While those authors analyzed the cumulative population of BeXRBs (Milky Way, LMC, and SMC), it is of interest to test the bimodality for the Galaxy alone. GBM allowed us to constrain the ephemerides for a large number of such transients over the last decade, allowing us to probe the spin period distribution of BeXRBs in the Galaxy. This is shown in Figure 4, which shows two distinct distributions peaking at ~ 10 and ~ 200 s with a clear gap at ~ 40 s, confirming the findings of Knigge et al. (2011).

7.2. Accretion-driven Torques

We analyzed the relationship between the spin-up strength and the observed luminosity for all of the GBM XRP sources. As a measure of the spin-up strength, we calculated the peak luminosity of the brightest outburst ever recorded over GBM lifetime for a given source, and compared it with the corresponding maximum spin period derivative calculated over the same outburst. This allows us to study the dependence of these two parameters according to the Ghosh–Lamb (GL) model expressed by Equation (10). For a meaningful comparison of the torque strength as a function of the luminosity, we considered the bolometric (0.1–200 keV) luminosity inferred for each inferred source, as described in the Appendix A.

Our results are shown in Figure 5, together with theoretical predictions from Equation (10). The figure clearly shows a correlation, where the behavior of the measured sources mostly follows the predictions from the GL model. The model predicts different spin equilibrium values, $n(\omega_s) = 0$, for different magnetic field strengths. The spin equilibrium is characterized by a cuspid in the GL function and discriminates between the fast rotator regime ($\omega_s > 1$, to the left side of the cuspid) where the source is spinning down, and the slow rotator regime ($\omega_s < 1$, to the right side of the cuspid) where the source is spinning up. Deviations of up to a factor of three have been highlighted by Sugizaki et al. (2017) between observations of spin-up rates and predictions from the GL model. However, the observed deviations were most likely ascribed to the uncertainty in the involved parameters, in particular the distance, d . Thanks to the Gaia DR2 (see Appendix B), we have been able to sensibly reduce the uncertainty on this parameter and compare the model predictions with the most precise data currently available. An example of how improved distances help with our understanding of source behavior is especially pertinent to sources like V 0332+53 (X 0331+53). Sugizaki et al. (2017) find that the deviation of this source from theoretical predictions is anomalously high, concluding that its

⁵⁰ <https://gammaray.msfc.nasa.gov/gbm/science/pulsars/lightcurves/gx1p4.html>

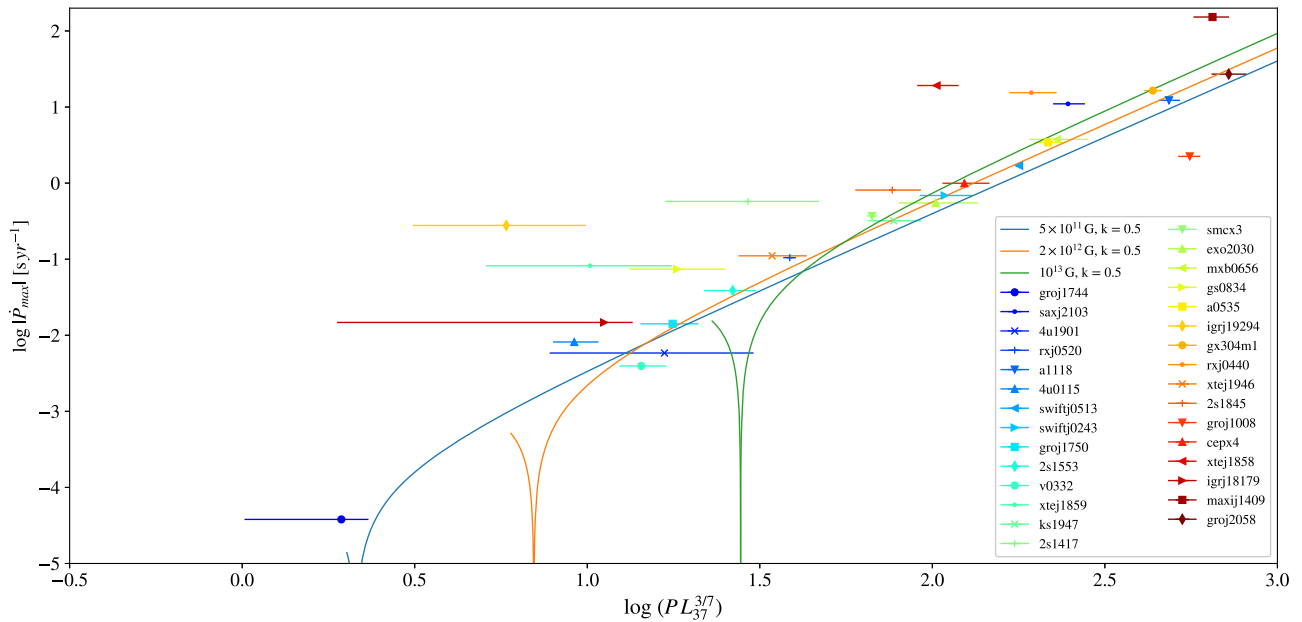


Figure 5. Distribution of the maximum spin period derivative (absolute value) against the maximum peak bolometric luminosity normalized to the source spin period ($PL_{37}^{3/7}$) for all GBM transient sources. The turquoise, orange, and green continuous lines correspond to the GL model (Equation (10)) for different magnetic field values, i.e., 5×10^{11} , 2×10^{12} , and 10^{13} G, respectively (all assuming a coupling factor of $k = 0.5$). Model cusps mark the value of the dimensionless parameter n ($\omega_s = 0$). Despite the lack of an orbital solution, the following sources have been included in the plot: MXB 0656–072, GS 0834–430, IGR J19294+1816, RX J0440.9+4431, Cep X-4, XTE J1858+034, GRO J1008–57, IGR J18179–1621, MAXI J1409–619, and GRO J2058+42.

behavior is due to an overestimate of the source distance. An improved distance obtained by Gaia ($5.1_{-0.8}^{+1.1}$ kpc) was able to better constrain the source’s behavior. Although marginal deviation is still present between observations and the torque model, the difference is significant only at the 1σ c.l. While the majority of the Gaia distances in this paper are consistent with previous measurements, there are some sources in this work that are inconsistent with distance values estimated through other methods, e.g., by adopting the luminosity dependence of the spin-up rate (see Equation (10)). Such a discrepancy is likely due to a combination of factors, including the uncertainty in the physical mechanisms driving the spin evolution of accreting NSs, the poorly constrained parameters of Equation (10), and the limited range over which Gaia can measure distances. The latter implies that more reliable distances can be obtained for measured parallaxes that are smaller than their uncertainties, i.e., usually below ~ 5 kpc (Bailer-Jones et al. 2018; Luri et al. 2018).

Even considering the Gaia measured distances, a few sources still show considerable deviations from the GL model. Some of these have unknown or poorly known orbital solutions, namely GS 0834–430, IGR J19294+1816, RX J0440.9+4431, XTE J1858+034, IGR J18179–1621, MAXI J1409–619, GRO J1008–57, and GRO J2058+42. Some of the deviation is due to the lack of a timing solution; although, a few binary systems with known orbital solutions have also been observed to deviate from the GL model predictions, e.g., 4U 0115+634 and 2S 1417–624. Recently, Ji et al. (2020) analyzed a 2018 outburst from 2S 1417–624 that employed a standard GL model to account for the spin-up shown by the source during the accretion episode. However, they had to use a coupling parameter value of $k \sim 0.3$ and a distance of 20 kpc in order to achieve a good fit. We find that a standard value of the coupling constant ($k \sim 0.5$) and a measured Gaia distance of ~ 10 kpc is

unable to account for the observed spin-up from that outburst (see Figure 5), in agreement with findings from Ji et al. (2020).

7.3. Improvement/Finding of Orbital Solutions

Following the technique described in Section 4, we derived or updated ephemerides for a selected sample of sources: 4U 0115+63, 4U 1901+03, and 2S 1553–542. To separate the pulsar emission from the background, good CTIME data are represented by Fourier components while a background model is fit to the data and then subtracted. The background model includes bright known sources, the variation in the detector responses, the Earth occultation steps, and a remaining long-term background contribution. Details on this procedure are described in Finger et al. (1999), Camero-Arranz et al. (2010a), and Jenke et al. (2012b).

The observed times are barycentered using the JPL Planetary ephemeris DE200 catalog (Standish 1990). The barycentered times (TBD) are modulated by the binary orbital motion of the emitting pulsar, $t^{\text{em}} = \text{TDB} - z$, and the binary orbital parameters can be constrained by fitting the TBD times to Equation (14) (starting from an approximate, previously known solution). Orbital fits were obtained for two HMXBs due to their X-ray duty cycle. Best-fit orbital elements for those sources are presented in Table 1.

8. Summary

We have summarized more than 10 yr of Fermi/GBM accreting X-ray pulsars observations as part of the GAPP. Detailed inspection of the spin history of accreting XRP’s unveils a plethora of differences, highlighting the importance of continuous, wide-field monitoring observations. We showed how GBM observations are vital in addressing decade-long behaviors, such as long-term cycles in the Be disks (e.g., in EXO 2030+375) and torque reversals (e.g., in 2S 1845–024). Adherence of accretion-driven torques to the GL model for all

GBM detected transient systems, as well as quasi-spherical accretion torques model predictions for a subsample of wind-accreting systems, have been tested, aided by updated source distances from Gaia DR2. This has allowed us to test the model predictions and to cross-check independent distance determinations (e.g., 2S 1417–624). Finally, we obtained new/updated orbital solutions for three accreting XRPs. Our results demonstrate the capabilities of GBM as an excellent instrument for monitoring accreting X-ray pulsars and its important scientific contribution to this field.

We dedicate this paper to Dr. Mark Finger, retired, who initiated the GBM Accreting Pulsars Program and was an irreplaceable part of it.

This research has made use of data and software provided by the High Energy Astrophysics Science Archive Research Center (HEASARC), which is a service of the Astrophysics Science Division at NASA/GSFC and the High Energy Astrophysics Division of the Smithsonian Astrophysical Observatory. We acknowledge extensive use of the NASA Abstract Database Service (ADS). C.M. is supported by an appointment to the NASA Postdoctoral Program at the Marshall Space Flight Center, administered by Universities Space Research Association under contract with NASA.

Facilities: Fermi/GBM, CGRO/BATSE, Swift/BAT.

Software: HEASoft.

Appendix A The Bolometric Luminosity

The GL model provides the spin/torque occurring on a source that accretes matter producing a certain luminosity. The luminosity considered in that model is a bolometric quantity in the X-ray domain, i.e., over the entire 0.1–200 keV energy band. However, it is rare that spectral data can offer such a wide energy coverage. Even so, the spectral energy distribution of accreting X-ray pulsars is rapidly folding beyond ~ 20 keV, and the flux measurement becomes progressively more uncertain at higher energies. Therefore, a different approach in deriving the luminosity at energies that differ from the band covered by the observing instrument must be taken.

A common approach is to evaluate the spectral model over a given energy range and then extend it to cover the 0.1–200 keV energy range. This approach assumes that the inferred spectral model shows no variations with respect to the model that was originally fit to the actual data. This is not always true, since additional spectral components sometimes emerge at different energies or luminosity states. However, the spectrum between 1 and 20 keV is thought to be the most representative because it is sufficient to characterize the cutoff power-law component, the column density absorption, and, possibly, an additional soft component (e.g., the blackbody component coming from the accretion disk).

In this work, we followed the same strategy. For each source, we first considered the best-fit models in the 1–20 keV found in literature (see Table 1), describing the source spectrum at the highest observed luminosity. Successively, the model was extended to the bolometric energy band through the employment of a dummy response using XSPEC.⁵¹ We are aware that this procedure introduces systematic uncertainty in the peak

luminosity derivation, due to the possible emergence of additional spectral components at energies beyond the interval in which the best-fit model is calculated. However, the estimated uncertainty in the flux derivation from this procedure is 15% (see also Coti Zelati et al. 2018). This is a relatively low value when compared with the uncertainty in the luminosity calculation derived from the high uncertainty on the source distance that still holds for some sources.

Appendix B The GAIA Distances

On 2018 April 25, the GAIA Data Release 2 (DR2) was made available (Gaia Collaboration et al. 2018). Soon after, an online catalog⁵² was also made available by the Gaia team to list the distances for a large number of sources, based on the priors employed by Bailer-Jones et al. (2018). To derive the most updated available distances for the sources in Table 1, we adopted the following procedure:

1. Query the “Single Source Search” catalog for the source name as reported in Table 1 (This catalog is based on the SIMBAD astronomical database Wenger et al. 2000).
2. Retrieve the corresponding Gaia ID. Only Gaia DR2 IDs have been used in this work (unless otherwise stated).
3. Query the Table Access Protocol (TAP) for the distance of the correspondent Gaia ID, as recommended in Section 4 of Bailer-Jones et al. (2018).

We report the angular offset between the closest Gaia counterpart and each source nominal position when the offset is larger than $3''.5$ (the typical systematic error for Swift/XRT positions⁵³).

ORCID iDs

C. Malacaria  <https://orcid.org/0000-0002-0380-0041>

C. A. Wilson-Hodge  <https://orcid.org/0000-0002-8585-0084>

References

- Abarr, Q., Baring, M., Beheshtipour, B., et al. 2020, *ApJ*, **891**, 70
Aoki, T., Dotani, T., Ebisawa, K., et al. 1992, *PASJ*, **44**, 641
Apparao, K. M. V., Naranan, S., Kelley, R. L., & Bradt, H. V. 1980, *A&A*, **89**, 249
Arons, J., & Lea, S. M. 1976, *ApJ*, **207**, 914
Ash, T. D. C., Reynolds, A. P., Roche, P., et al. 1999, *MNRAS*, **307**, 357
Audley, M. D., Nagase, F., Mitsuda, K., Angelini, L., & Kelley, R. L. 2006, *MNRAS*, **367**, 1147
Bailer-Jones, C. A. L., Rybizki, J., Fouesneau, M., Mantelet, G., & Andrae, R. 2018, *AJ*, **156**, 58
Ballhausen, R., Kühnel, M., Pottschmidt, K., et al. 2016, *A&A*, **591**, A65
Baykal, A. 1997, *A&A*, **319**, 515
Baykal, A., Inam, S. Ç., & Beklen, E. 2006, *A&A*, **453**, 1037
Baykal, A., Inam, S. Ç., Stark, M. J., et al. 2007, *MNRAS*, **374**, 1108
Bessolaz, N., Zanni, C., Ferreira, J., Keppens, R., & Bouvier, J. 2008, *A&A*, **478**, 155
Bikmaev, I., Shimansky, V., Irtuganov, E., et al. 2017, *ATel*, **10968**, 1
Bildsten, L., Chakrabarty, D., Chiu, J., et al. 1994, in *AIP Conf. Ser.* 304, The Second Compton Symp., ed. C. E. Fichtel, N. Gehrels, & J. P. Norris (Melville, NY: AIP), 290
Bildsten, L., Chakrabarty, D., Chiu, J., et al. 1997, *ApJS*, **113**, 367
Blondin, J. M. 2013, *ApJ*, **767**, 135
Blondin, J. M., & Raymer, E. 2012, *ApJ*, **752**, 30
Blondin, J. M., Stevens, I. R., & Kallman, T. R. 1991, *ApJ*, **371**, 684

⁵¹ The dummyrsp tool, <https://heasarc.gsfc.nasa.gov/xanadu/xspec/manual/node94.html>.

⁵² <http://gaia.ari.uni-heidelberg.de/tap.html>

⁵³ <http://www.swift.ac.uk/analysis/xrt/xrtcentroid.php>

- Boldin, P. A., Tsygankov, S. S., & Lutovinov, A. A. 2013, *AstL*, **39**, 375
- Bonnet-Bidaud, J. M., & Mouchet, M. 1998, *A&A*, **332**, L9
- Borozdin, K., Gilfanov, M., Sunyaev, R., et al. 1990, *SvAL*, **16**, 345
- Bozzo, E., Falanga, M., & Stella, L. 2008, *ApJ*, **683**, 1031
- Bozzo, E., Ferrigno, C., Falanga, M., & Walter, R. 2011, *A&A*, **531**, A65
- Bozzo, E., Ferrigno, C., Türler, M., Manousakis, A., & Falanga, M. 2012, *A&A*, **545**, A83
- Bozzo, E., Oskinova, L., Feldmeier, A., & Falanga, M. 2016, *A&A*, **589**, A102
- Bozzo, E., Stella, L., Vietri, M., & Ghosh, P. 2009, *A&A*, **493**, 809
- Brucato, R. J., & Kristian, J. 1972, *ApJL*, **173**, L105
- Caballero, I., & Wilms, J. 2012, *MmSAI*, **83**, 230
- Camero-Arranz, A., Finger, M. H., Ikhsanov, N. R., Wilson-Hodge, C. A., & Beklen, E. 2010a, *ApJ*, **708**, L500
- Camero-Arranz, A., Finger, M. H., & Jenke, P. 2010b, *ATel*, **3069**, 1
- Camero-Arranz, A., Finger, M. H., Wilson-Hodge, C. A., et al. 2012, *ApJ*, **754**, 20
- Camero Arranz, A., Wilson, C. A., Finger, M. H., & Reglero, V. 2007, *A&A*, **473**, 551
- Chakrabarty, D. 1998, *ApJ*, **492**, 342
- Chakrabarty, D., Bildsten, L., Grunsfeld, J. M., et al. 1997, *ApJ*, **474**, 414
- Chakrabarty, D., Grunsfeld, J. M., Prince, T. A., et al. 1993, *ApJL*, **403**, L33
- Chakrabarty, D., Koh, T., Bildsten, L., et al. 1995, *ApJ*, **446**, 826
- Chakrabarty, D., & Roche, P. 1997, *ApJ*, **489**, 254
- Chakrabarty, D., Wang, Z., Juett, A. M., Lee, J. C., & Roche, P. 2002, *ApJ*, **573**, 789
- Cheng, Z.-Q., Shao, Y., & Li, X.-D. 2014, *ApJ*, **786**, 128
- Chevalier, C., & Ilovaisky, S. A. 1975, *IAUC*, **2778**, 1
- Clark, G., Dossy, R., Li, F., Jernigan, J. G., & van Paradijs, J. 1978, *ApJL*, **221**, L37
- Clark, G. W. 2000, NASA STI/Recon Technical Report N, 11066
- Clark, G. W., Schmidt, G. D., & Angel, J. R. P. 1975, *IAUC*, **2843**, 1
- Coe, M. J., Bird, A. J., Hill, A. B., et al. 2007, *MNRAS*, **378**, 1427
- Coe, M. J., Carpenter, G. F., Engel, A. R., & Quenby, J. J. 1975, *Natur*, **256**, 630
- Coe, M. J., Finger, M., Bartlett, E. S., & Udalski, A. 2015, *MNRAS*, **447**, 1630
- Coe, M. J., Negueruela, I., Buckley, D. A. H., Haigh, N. J., & Laycock, S. G. T. 2001, *MNRAS*, **324**, 623
- Coe, M. J., Roche, P., Everall, C., et al. 1994a, *MNRAS*, **270**, L57
- Coe, M. J., Roche, P., Everall, C., et al. 1994b, *A&A*, **289**, 784
- Cominsky, L., Clark, G. W., Li, F., Mayer, W., & Rappaport, S. 1978, *Natur*, **273**, 367
- Corbet, R., Marshall, F. E., & Markwardt, C. B. 2001, *IAUC*, **7562**, 1
- Corbet, R. H. D. 1986, *MNRAS*, **220**, 1047
- Corbet, R. H. D., Charles, P. A., & van der Klis, M. 1986, *A&A*, **162**, 117
- Corbet, R. H. D., in't Zand, J. J. M., Levine, A. M., & Marshall, F. E. 2009, *ApJ*, **695**, 30
- Corbet, R. H. D., & Krimm, H. A. 2009, *ATel*, **2008**, 1
- Corbet, R. H. D., Laycock, S., Coe, M. J., Marshall, F. E., & Markwardt, C. B. 2004, in AIP Conf. Ser. 714, X-ray Timing 2003: Rossi and Beyond, ed. P. Kaaret, F. K. Lamb, & J. H. Swank (Melville, NY: AIP), 337
- Corbet, R. H. D., Sokoloski, J. L., Mukai, K., Markwardt, C. B., & Tueller, J. 2008, *ApJ*, **675**, 1424
- Corbet, R. H. D., Woo, J. W., & Nagase, F. 1993, *A&A*, **276**, 52
- Coti Zelati, F., Rea, N., Pons, J. A., Campana, S., & Esposito, P. 2018, *MNRAS*, **474**, 961
- Court, J. M. C., Altamirano, D., Albayati, A. C., et al. 2018, *MNRAS*, **481**, 2273
- Cusumano, G., Segreto, A., La Parola, V., et al. 2016, arXiv:1601.08138
- Cutler, E. P., Dennis, B. R., & Dolan, J. F. 1986, *ApJ*, **300**, 551
- Dall'Osso, S., Perma, R., Papitto, A., Bozzo, E., & Stella, L. 2016, *MNRAS*, **457**, 3076
- D'Ai, A., Di Salvo, T., Iaria, R., et al. 2015, *MNRAS*, **449**, 4288
- Davidson, K., & Ostriker, J. P. 1973, *ApJ*, **179**, 585
- Davison, P. J. N., Watson, M. G., & Pye, J. P. 1977, *MNRAS*, **181**, 73P
- de Kool, M., & Anzer, U. 1993, *MNRAS*, **262**, 726
- Deeter, J. E., Boynton, P. E., Lamb, F. K., & Zylstra, G. 1989, *ApJ*, **336**, 376
- Deeter, J. E., Boynton, P. E., & Pravdo, S. H. 1981, *ApJ*, **247**, 1003
- Domček, V., van den Eijnden, J., Escorial, A. R., et al. 2019, *ATel*, **13215**, 1
- Doroshenko, R., Santangelo, A., Doroshenko, V., & Piraino, S. 2017, *A&A*, **600**, A52
- Doroshenko, V., Santangelo, A., Suleimanov, V., et al. 2010a, *A&A*, **515**, A10
- Doroshenko, V., Suchy, S., Santangelo, A., et al. 2010b, *A&A*, **515**, L1
- Doroshenko, V., Tsygankov, S., & Santangelo, A. 2016, *A&A*, **589**, A72
- Doroshenko, V., Zhang, S. N., Santangelo, A., et al. 2020, *MNRAS*, **491**, 1857
- Doty, J. P., Lewin, W. H. G., & Hoffman, J. A. 1981, *ApJ*, **243**, 257
- Ducci, L., Sidoli, L., Paizis, A., Mereghetti, S., & Pizzochero, P. M. 2008, in Proc. of the 7th INTEGRAL Workshop (Copenhagen) **116**
- Edge, W. R. T., Coe, M. J., Galache, J. L., et al. 2004, *MNRAS*, **353**, 1286
- El Mellah, I., Sander, A. A. C., Sundqvist, J. O., & Keppens, R. 2019, *A&A*, **622**, A189
- Epili, P., Naik, S., & Jaisawal, G. K. 2016, *RAA*, **16**, 77
- Fabian, A. C., Pringle, J. E., & Webbink, R. F. 1975, *Natur*, **255**, 208
- Fabian, A. C., Pringle, J. E., & Webbink, R. F. 1976, *ApSS*, **42**, 161
- Falanga, M., Bozzo, E., Lutovinov, A., et al. 2015, *A&A*, **577**, A130
- Ferrigno, C., Farinelli, R., Bozzo, E., et al. 2013, *A&A*, **553**, A103
- Ferrigno, C., Segreto, A., Santangelo, A., et al. 2007, *A&A*, **462**, 995
- Finger, M. H., & Beklen, E. 2009, *ATel*, **2023**, 1
- Finger, M. H., Bildsten, L., Chakrabarty, D., et al. 1999, *ApJ*, **517**, 449
- Finger, M. H., Jenke, P. A., & Wilson-Hodge, C. 2015, *ATel*, **7045**, 1
- Finger, M. H., Koh, D. T., Nelson, R. W., et al. 1996a, *Natur*, **381**, 291
- Finger, M. H., Wilson, R. B., & Chakrabarty, D. 1996b, *A&AS*, **120**, 209
- Finger, M. H., Wilson, R. B., & Harmon, B. A. 1996c, *ApJ*, **459**, 288
- Finger, M. H., & Wilson-Hodge, C. A. 2012, *ATel*, **3961**, 1
- Fishman, G. J., Meegan, C. A., Wilson, R. B., Paciesas, W. S., & Pendleton, G. N. 1992, in NASA Conf. Publication 3137, 26
- Forman, W., Jones, C., & Tananbaum, H. 1976, *ApJL*, **206**, L29
- Fryxell, B. A., & Taam, R. E. 1988, *ApJ*, **335**, 862
- Fürst, F., Pottschmidt, K., Wilms, J., et al. 2014, *ApJ*, **780**, 133
- Gaia Collaboration, Brown, A. G. A., Vallenari, A., et al. 2018, *A&A*, **616**, A1
- Galloway, D. K., Morgan, E. H., & Levine, A. M. 2004, *ApJ*, **613**, 1164
- Galloway, D. K., Wang, Z., & Morgan, E. H. 2005, *ApJ*, **635**, 1217
- Gehrels, N., Chipman, E., & Kniffen, D. 1994, *ApJS*, **92**, 351
- Ghosh, P., & Lamb, F. K. 1979a, *ApJ*, **232**, 259
- Ghosh, P., & Lamb, F. K. 1979b, *ApJ*, **234**, 296
- Ghosh, P., Lamb, F. K., & Pethick, C. J. 1977, *ApJ*, **217**, 578
- Giacconi, R., Gursky, H., Kellogg, E., Schreier, E., & Tananbaum, H. 1971, *ApJL*, **167**, L67
- Giacconi, R., Murray, S., Gursky, H., et al. 1972, *ApJ*, **178**, 281
- Giangrande, A., Giovannelli, F., Bartolini, C., Guarnieri, A., & Piccioni, A. 1980, *A&AS*, **40**, 289
- Giménez-García, A., Shenar, T., Torrejón, J. M., et al. 2016, *A&A*, **591**, A26
- Glass, I. S., & Feast, M. W. 1973, *NPhS*, **245**, 39
- González-Galán, A., Kuulkers, E., Kretschmar, P., et al. 2012, *A&A*, **537**, A66
- González-Galán, A., Oskinova, L. M., Popov, S. B., et al. 2018, *MNRAS*, **475**, 2809
- Gosling, A. J., Bandyopadhyay, R. M., Miller-Jones, J. C. A., & Farrell, S. A. 2007, *MNRAS*, **380**, 1511
- Grindlay, J. E., Petro, L. D., & McClintock, J. E. 1984, *ApJ*, **276**, 621
- Gupta, S., Naik, S., Jaisawal, G. K., & Epili, P. R. 2018, *MNRAS*, **479**, 5612
- Güver, T., Özel, F., Cabrera-Lavers, A., & Wroblewski, P. 2010, *ApJ*, **712**, 964
- Halpern, J. P. 2012, *ATel*, **3949**, 1
- Halpern, J. P., & Levine, A. M. 2019, *ATel*, **12519**, 1
- Hammerschlag-Hensberge, G., Zuiderwijk, E. J., De Loore, C., & van den Heuvel, E. P. J. 1979, *A&A*, **76**, 245
- Harmon, B. A., Wilson, C. A., Fishman, G. J., et al. 2004, *ApJS*, **154**, 585
- Hilditch, R. W. 2001, An Introduction to Close Binary Stars (Cambridge: Cambridge Univ. Press)
- Hill, A. B., Bird, A. J., Dean, A. J., et al. 2007, *MNRAS*, **381**, 1275
- Hiltner, W. A., Werner, J., & Osmer, P. 1972, *ApJL*, **175**, L19
- Hinkle, K. H., Fekel, F. C., Joyce, R. R., et al. 2006, *ApJ*, **641**, 479
- Ho, W. C. G., Klus, H., Coe, M. J., & Andersson, N. 2014, *MNRAS*, **437**, 3664
- Honeycutt, R. K., & Schlegel, E. M. 1985, *PASP*, **97**, 300
- Hulleman, F., in 't Zand, J. J. M., & Heise, J. 1998, *A&A*, **337**, L25
- Hutchings, J. B., Bernard, J. E., Crampton, D., & Cowley, A. P. 1978, *ApJ*, **223**, 530
- Hutchings, J. B., Cowley, A. P., Crampton, D., van Paradijs, J., & White, N. E. 1979, *ApJ*, **229**, 1079
- Illarionov, A. F., & Sunyaev, R. A. 1975, *A&A*, **39**, 185
- İnam, S. Ç., Baykal, A., Matthew Scott, D., Finger, M., & Swank, J. 2004, *MNRAS*, **349**, 173
- Iping, R. C., & Petterson, J. A. 1990, *A&A*, **239**, 221
- Israel, G. L., Covino, S., Campana, S., et al. 2000, *MNRAS*, **314**, 87
- Ives, J. C., Sanford, P. W., & Bell Burnell, S. J. 1975, *Natur*, **254**, 578
- Jaisawal, G. K., Wilson-Hodge, C. A., Fabian, A. C., et al. 2019, *ApJ*, **885**, 18
- Janot-Pacheco, E., Ilovaisky, S. A., & Chevalier, C. 1981, *A&A*, **99**, 274
- Jenke, P., & Finger, M. H. 2011, *ATel*, **3839**, 1
- Jenke, P., Finger, M. H., & Connaughton, V. 2012a, *ATel*, **4235**, 1
- Jenke, P., & Wilson-Hodge, C. A. 2017, *ATel*, **10812**, 1
- Jenke, P., Wilson-Hodge, C. A., & Malacaria, C. 2018a, *ATel*, **11700**, 1
- Jenke, P., Wilson-Hodge, C. A., & Malacaria, C. 2018b, *ATel*, **11280**, 1

- Jenke, P. A., Finger, M. H., Wilson-Hodge, C. A., & Camero-Arranz, A. 2012b, *ApJ*, **759**, 124
- Ji, L., Doroshenko, V., Santangelo, A., et al. 2020, *MNRAS*, **491**, 1851
- Kaper, L., Hammerschlag-Hensberge, G., & Zuiderwijk, E. J. 1994, *A&A*, **289**, 846
- Kaper, L., Lamers, H. J. G. L. M., Ruymaekers, E., van den Heuvel, E. P. J., & Zuiderwijk, E. J. 1995, *A&A*, **300**, 446
- Kaper, L., van der Meer, A., & Najarro, F. 2006, *A&A*, **457**, 595
- Kelley, R. L., Apparao, K. M. V., Doxsey, R. E., et al. 1981, *ApJ*, **243**, 251
- Kelley, R. L., Ayasli, S., & Rappaport, S. 1982, *IAUC*, **3667**, 3
- Kelley, R. L., Rappaport, S., & Ayasli, S. 1983a, *ApJ*, **274**, 765
- Kelley, R. L., Rappaport, S., Clark, G. W., & Petro, L. D. 1983b, *ApJ*, **268**, 790
- Kennea, J. A., Curran, P., Krimm, H., et al. 2010, *ATel*, **3060**, 1
- Kennea, J. A., Krimm, H. A., Page, K. L., & Tohuvavohu, A. 2019, *GCN*, **23882**, 1
- Kennea, J. A., Lien, A. Y., Krimm, H. A., Cenko, S. B., & Siegel, M. H. 2017, *ATel*, **10809**, 1
- Kim, V. Y., & Ikhsanov, N. R. 2017, *Journal of Physics Conference Series*, **929**, 012005
- Klochkov, D., Staubert, R., Postnov, K., Shakura, N., & Santangelo, A. 2009, *A&A*, **506**, 1261
- Klus, H., Bartlett, E. S., Bird, A. J., et al. 2013, *MNRAS*, **428**, 3607
- Klus, H., Ho, W. C. G., Coe, M. J., Corbet, R. H. D., & Townsend, L. J. 2014, *MNRAS*, **437**, 3863
- Knigge, C., Coe, M. J., & Podsiadlowski, P. 2011, *Natur*, **479**, 372
- Koenigsberger, G., Moreno, E., & Harrington, D. M. 2012, *A&A*, **539**, A84
- Koh, D. T., Bildsten, L., Chakrabarty, D., et al. 1997, *ApJ*, **479**, 933
- Kotze, M. M., & Charles, P. A. 2012, *MNRAS*, **420**, 1575
- Kouveliotou, C., van Paradijs, J., Fishman, G. J., et al. 1996, *Natur*, **379**, 799
- Koyama, K., Kunieda, H., Takeuchi, Y., & Tawara, Y. 1990, *PASJ*, **42**, L59
- Kreykenbohm, I., Wilms, J., Coburn, W., et al. 2004, *A&A*, **427**, 975
- Kreykenbohm, I., Wilms, J., Kretschmar, P., et al. 2008, *A&A*, **492**, 511
- Krimm, H. A., Barthelmy, S. D., Baumgartner, W., et al. 2010, *ATel*, **2846**, 1
- Krimm, H. A., Corbet, R. H. D., Evans, P. A., et al. 2009, *ATel*, **2011**, 1
- Krzeminski, W. 1974, *ApJL*, **192**, L135
- Kuehnelt, M. 2016, PhD thesis, Friedrich-Alexander-Universität Erlangen-Nürnberg
- Kuehnelt, M., Finger, M. H., Fuerst, F., et al. 2014, *ATel*, **5856**, 1
- Kühnel, M., Fürst, F., Pottschmidt, K., et al. 2017, *A&A*, **607**, A88
- Kühnel, M., Müller, S., Kreykenbohm, I., et al. 2013, *A&A*, **555**, A95
- Kulkarni, A. K., & Romanova, M. M. 2008, *MNRAS*, **386**, 673
- Lamb, F. K., Pethick, C. J., & Pines, D. 1973, *ApJ*, **184**, 271
- Laplace, E., Mihara, T., Moritani, Y., et al. 2017, *A&A*, **597**, A124
- Laycock, S., Corbet, R. H. D., Coe, M. J., et al. 2003, *MNRAS*, **339**, 435
- Leahy, D. A., & Abdallah, M. H. 2014, *ApJ*, **793**, 79
- Leahy, D. A., & Igna, C. D. 2010, *ApJ*, **713**, 318
- Levine, A. M., & Corbet, R. 2006, *ATel*, **940**, 1
- Lewin, W. H. G., Ricker, G. R., & McClintock, J. E. 1971, *ApJL*, **169**, L17
- Lewin, W. H. G., van Paradijs, J., & van den Heuvel, E. P. J. 1997, *X-ray Binaries* (Cambridge: Cambridge Univ. Press)
- Li, F., Rappaport, S., Clark, G. W., & Jernigan, J. G. 1979, *ApJ*, **228**, 893
- Li, J., Wang, W., & Zhao, Y. 2012, *MNRAS*, **423**, 2854
- Li, X.-D. 1997, *ApJ*, **476**, 278
- Li, X.-D., & Wang, Z.-R. 1999, *ApJ*, **513**, 845
- Long, M., Romanova, M. M., & Lovelace, R. V. E. 2005, *ApJ*, **634**, 1214
- Luri, X., Brown, A. G. A., Sarro, L. M., et al. 2018, *A&A*, **616**, A9
- Lutovinov, A. A., Buckley, D. A. H., Townsend, L. J., Tsygankov, S. S., & Kennea, J. 2016, *MNRAS*, **462**, 3823
- Lutovinov, A. A., Tsygankov, S. S., Karasev, D. I., Molkov, S. V., & Doroshenko, V. 2019, *MNRAS*, **485**, 770
- Maitra, C. 2017, *JApA*, **38**, 50
- Makino, F., & GINGA Team 1988a, *IAUC*, **4661**, 2
- Makino, F., & GINGA Team 1988b, *IAUC*, **4577**, 1
- Makishima, K., Koyama, K., Hayakawa, S., & Nagase, F. 1987, *ApJ*, **314**, 619
- Makishima, K., Ohashi, T., Sakao, T., et al. 1988, *Natur*, **333**, 746
- Malacaria, C., Jenke, P., Wilson-Hodge, C. A., & Roberts, O. J. 2019, *ATel*, **12614**, 1
- Malacaria, C., Klochkov, D., Santangelo, A., & Staubert, R. 2015, *A&A*, **581**, A121
- Malacaria, C., Kollatschny, W., Whelan, E., et al. 2017, *A&A*, **603**, A24
- Malacaria, C., Mihara, T., Santangelo, A., et al. 2016, *A&A*, **588**, A100
- Mangano, V. 2009, *ATel*, **1896**, 1
- Marcu-Cheatham, D. M., Pottschmidt, K., Kühnel, M., et al. 2015, *ApJ*, **815**, 44
- Marshall, F. E., in 't Zand, J. J. M., Strohmayer, T., & Markwardt, C. B. 1999, *IAUC*, **7240**, 2
- Martínez-Núñez, S., Kretschmar, P., Bozzo, E., et al. 2017, *SSRv*, **212**, 59
- Masetti, N., D'Avanzo, P., Blagorodnova, N., & Palazzi, E. 2014, *ATel*, **5999**, 1
- Mason, A. B., Clark, J. S., Norton, A. J., Negueruela, I., & Roche, P. 2009, *A&A*, **505**, 281
- Mason, K. O., Murdin, P. G., Parkes, G. E., & Visvanathan, N. 1978, *MNRAS*, **184**, 45P
- McBride, V. A., Coe, M. J., Negueruela, I., Schurch, M. P. E., & McGowan, K. E. 2008, *MNRAS*, **388**, 1198
- McBride, V. A., Wilms, J., Coe, M. J., et al. 2006, *A&A*, **451**, 267
- McBride, V. A., Wilms, J., Kreykenbohm, I., et al. 2007, *A&A*, **470**, 1065
- McClintock, J. E., Bradt, H. V., Doxsey, R. E., et al. 1977a, *Natur*, **270**, 320
- McClintock, J. E., Li, F. K., Canizares, C. R., & Grindlay, J. E. 1980, *ApJL*, **235**, L81
- McClintock, J. E., Rappaport, S. A., Nugent, J. J., & Li, F. K. 1977b, *ApJL*, **216**, L15
- McCollum, B., & Laine, S. 2019, *ATel*, **12560**, 1
- Meegan, C., Lichti, G., Bhat, P. N., et al. 2009, *ApJ*, **702**, 791
- Middleditch, J., Mason, K. O., Nelson, J. E., & White, N. E. 1981, *ApJ*, **244**, 1001
- Molkov, S. V., Cherepashchuk, A. M., Revnivtsev, M. G., et al. 2004, *ATel*, **274**, 1
- Monageng, I. M., Coe, M. J., Townsend, L. J., et al. 2019, *MNRAS*, **485**, 4617
- Morgan, E., Remillard, R., & Swank, J. 2003, *ATel*, **199**, 1
- Motch, C., Stella, L., Janot-Pacheco, E., & Mouchet, M. 1991, *ApJ*, **369**, 490
- Müller, D., Klochkov, D., Caballero, I., & Santangelo, A. 2013, *A&A*, **552**, A81
- Nabizadeh, A., Mönkkönen, J., Tsygankov, S. S., et al. 2019, *A&A*, **629**, A101
- Nagase, F. 1989a, *PASJ*, **41**, 1
- Nagase, F. 1989b, in *Proc. of the 23rd ESLAB Symposium on Two Topics in X-Ray Astronomy*, ed. J. Hunt & B. Battrick (Noordwijk: ESA), **45**
- Nagase, F., Corbet, R. H. D., Day, C. S. R., et al. 1992, *ApJ*, **396**, 147
- Nagase, F., Hayakawa, S., Kunieda, H., et al. 1982, *ApJ*, **263**, 814
- Nakajima, M., Negoro, H., Mihara, T., et al. 2019, *ATel*, **12498**, 1
- Nakajima, M., Negoro, H., Serino, M., et al. 2018, *ATel*, **11479**, 1
- Nakajima, M., Sugizaki, M., Mihara, T., et al. 2014, *ATel*, **6819**, 1
- Negueruela, I., Israel, G. L., Marco, A., Norton, A. J., & Speziali, R. 2003, *A&A*, **397**, 739
- Negueruela, I., & Okazaki, A. T. 2001, *A&A*, **369**, 108
- Negueruela, I., Okazaki, A. T., Fabregat, J., et al. 2001, *A&A*, **369**, 117
- Negueruela, I., Roche, P., Fabregat, J., & Coe, M. J. 1999, *MNRAS*, **307**, 695
- Nespoli, E., Reig, P., & Zezas, A. 2012, *A&A*, **547**, A103
- Nishiuchi, M., Koyama, K., Maeda, Y., et al. 1999, *ApJ*, **517**, 436
- Nowak, M. A., Paizis, A., Rodríguez, J., et al. 2012, *ApJ*, **757**, 143
- Okazaki, A. T., & Negueruela, I. 2001, *A&A*, **377**, 161
- Orlandini, M., Frontera, F., Masetti, N., Sguera, V., & Sidoli, L. 2012, *ApJ*, **748**, 86
- Pahari, M., & Pal, S. 2012, *MNRAS*, **423**, 3352
- Pakull, M. W., Motch, C., & Negueruela, I. 2003, *ATel*, **202**, 1
- Parkes, G. E., Culhane, J. L., Mason, K. O., & Murdin, P. G. 1980, *MNRAS*, **191**, 547
- Parkes, G. E., Murdin, P. G., & Mason, K. O. 1978, *MNRAS*, **184**, 73P
- Parmar, A. N., White, N. E., Stella, L., Izzo, C., & Ferri, P. 1989, *ApJ*, **338**, 359
- Paul, B. 2017, *JApA*, **38**, 39
- Postnov, K., Shakura, N., Staubert, R., et al. 2013, *MNRAS*, **435**, 1147
- Postnov, K. A., Mironov, A. I., Lutovinov, A. A., et al. 2015, *MNRAS*, **446**, 1013
- Pradhan, P., Bozzo, E., & Paul, B. 2018, *A&A*, **610**, A50
- Press, W. H., Teukolsky, S. A., Vetterling, W. T., & Flannery, B. P. 1992, *Numerical Recipes in FORTRAN. The Art of Scientific Computing* (Cambridge: Cambridge Univ. Press)
- Pringle, J. E., & Rees, M. J. 1972, *A&A*, **21**, 1
- Raichur, H., & Paul, B. 2008a, *MNRAS*, **387**, 439
- Raichur, H., & Paul, B. 2008b, *ApJ*, **685**, 1109
- Raichur, H., & Paul, B. 2010a, *MNRAS*, **406**, 2663
- Raichur, H., & Paul, B. 2010b, *MNRAS*, **401**, 1532
- Rappaport, S., Clark, G. W., Cominsky, L., Joss, P. C., & Li, F. 1978, *ApJL*, **224**, L1
- Reig, P., & Coe, M. J. 1998, *MNRAS*, **294**, 118
- Reig, P., Kougentakis, T., & Papamastorakis, G. 2004a, *ATel*, **308**, 1
- Reig, P., Negueruela, I., Fabregat, J., et al. 2004b, *A&A*, **421**, 673
- Reig, P., Negueruela, I., Papamastorakis, G., Manousakis, A., & Kougentakis, T. 2005, *A&A*, **440**, 637
- Reig, P., & Roche, P. 1999, *MNRAS*, **306**, 100
- Reig, P., Zezas, A., & Gkouvelis, L. 2010, *A&A*, **522**, A107

- Remillard, R., Levine, A., Takeshima, T., et al. 1998, *IAUC*, **6826**, 2
- Reynolds, A. P., Quaintrell, H., Still, M. D., et al. 1997, *MNRAS*, **288**, 43
- Riquelme, M. S., Torrejón, J. M., & Negueruela, I. 2012, *A&A*, **539**, A114
- Rodes-Roca, J. J., Bernabeu, G., Magazzù, A., Torrejón, J. M., & Solano, E. 2018, *MNRAS*, **476**, 2110
- Rodriguez, J., Tomsick, J. A., Bodaghee, A., et al. 2009a, *A&A*, **508**, 889
- Rodriguez, J., Tuerler, M., Chaty, S., & Tomsick, J. A. 2009b, *ATel*, **1998**, 1
- Rosenberg, F. D., Eyles, C. J., Skinner, G. K., & Willmore, A. P. 1975, *Natur*, **256**, 628
- Rubin, B. C., Finger, M. H., Scott, D. M., & Wilson, R. B. 1997, *ApJ*, **488**, 413
- Şahiner, Ş., Serim, M. M., Baykal, A., & İnam, S. Ç. 2016, *MNRAS*, **456**, 845
- Sanna, A., Riggio, A., Burderi, L., et al. 2017, *MNRAS*, **469**, 2
- Sartore, N., Jourdain, E., & Roques, J. P. 2015, *ApJ*, **806**, 193
- Sato, N., Nagase, F., Kawai, N., et al. 1986, *ApJ*, **304**, 241
- Schmidtke, P. C., Cowley, A. P., Frattare, L. M., et al. 1994, *PASP*, **106**, 843
- Schulz, N. S., Chakrabarty, D., & Marshall, H. L. 2019, arXiv:1911.11684
- Scott, D. M., Finger, M. H., Wilson, R. B., et al. 1997, *ApJ*, **488**, 831
- Scott, D. M., Leahy, D. A., & Wilson, R. B. 2000, *ApJ*, **539**, 392
- Shakura, N., & Postnov, K. 2017, arXiv:1702.03393
- Shakura, N., Postnov, K., & Hjalmarsdotter, L. 2013, *MNRAS*, **428**, 670
- Shakura, N., Postnov, K., Kochetkova, A., & Hjalmarsdotter, L. 2012, *MNRAS*, **420**, 216
- Shakura, N. I., Postnov, K. A., Kochetkova, A. Y., & Hjalmarsdotter, L. 2014, in *EPJ Web of Conf.*, Vol. 64, Physics at the Magnetospheric Boundary (Les Ulis: EDP Sciences), 02001
- Shaw, S. E., Hill, A. B., Kuulkers, E., et al. 2009, *MNRAS*, **393**, 419
- Sidoli, L., & Paizis, A. 2018, *MNRAS*, **481**, 2779
- Sidoli, L., Paizis, A., Fürst, F., et al. 2015, *MNRAS*, **447**, 1299
- Smith, D. A., Takeshima, T., Wilson, C. A., et al. 1998, *IAUC*, **7014**, 1
- Sootome, T., Nakajima, M., Mihara, T., et al. 2011, *ATel*, **3829**, 1
- Standish, E. M., Jr. 1990, *A&A*, **233**, 252
- Staubert, R., Klochkov, D., & Wilms, J. 2009, *A&A*, **500**, 883
- Staubert, R., Pottschmidt, K., Doroshenko, V., et al. 2011, *A&A*, **527**, A7
- Steele, I. A., Negueruela, I., Coe, M. J., & Roche, P. 1998, *MNRAS*, **297**, L5
- Stella, L., White, N. E., Davelaar, J., et al. 1985, *ApJL*, **288**, L45
- Stollberg, M. T., Finger, M. H., Wilson, R. B., et al. 1993, *IAUC*, **5836**, 1
- Strader, J., Chomiuk, L., Swihart, S., & Aydi, E. 2019, *ATel*, **12554**, 1
- Strohmayer, T. E., Guillot, S., Vasilopoulos, G., et al. 2018, *ATel*, **12222**, 1
- Sturm, R., Carpano, S., Haberl, F., Maggi, P., & Vasilopoulos, G. 2014, *ATel*, **6483**, 1
- Suchy, S., Pottschmidt, K., Rothschild, R. E., et al. 2011, *ApJ*, **733**, 15
- Sugizaki, M., Mihara, T., Nakajima, M., & Makishima, K. 2017, *PASJ*, **69**, 100
- Sugizaki, M., Yamamoto, T., Mihara, T., Nakajima, M., & Makishima, K. 2015, *PASJ*, **67**, 73
- Swank, J., & Morgan, E. 2000, *IAUC*, **7531**, 4
- Takeshima, T., Corbet, R. H. D., Marshall, F. E., Swank, J., & Chakrabarty, D. 1998, *IAUC*, **6826**, 1
- Tananbaum, H., Gursky, H., Kellogg, E. M., et al. 1972, *ApJL*, **174**, L143
- Thompson, T. W. J., & Rothschild, R. E. 2009, *ApJ*, **691**, 1744
- Tjemkes, S. A., van Paradijs, J., & Zuiderwijk, E. J. 1986, *A&A*, **154**, 77
- Townsend, L. J., Kennea, J. A., Coe, M. J., et al. 2017, *MNRAS*, **471**, 3878
- Tsunemi, H., Kitamoto, S., & Tamura, K. 1996, *ApJ*, **456**, 316
- Tsygankov, S. S., Lutovinov, A. A., Krivonos, R. A., et al. 2016, *MNRAS*, **457**, 258
- Tuerler, M., Chenevez, J., Bozzo, E., et al. 2012, *ATel*, **3947**, 1
- Turler, M., Rodriguez, J., & Ferrigno, C. 2009, *ATel*, **1997**, 1
- Usui, R., Morii, M., Kawai, N., et al. 2012, *PASJ*, **64**, 79
- van Kerkwijk, M. H., van Paradijs, J., Zuiderwijk, E. J., et al. 1995, *A&A*, **303**, 483
- Vasilopoulos, G., Haberl, F., Sturm, R., Maggi, P., & Udalski, A. 2014, *A&A*, **567**, A129
- Vasilopoulos, G., Sturm, R., Maggi, P., & Haberl, F. 2013, *ATel*, **5673**, 1
- Verrecchia, F., Israel, G. L., Negueruela, I., et al. 2002, *A&A*, **393**, 983
- Vidal, N. V. 1973, *ApJL*, **186**, L81
- Walter, R., & Ferrigno, C. 2017, in *Handbook of Supernovae*, ed. A. Alsabti & P. Murdin (Cham: Springer)
- Walter, R., Lutovinov, A. A., Bozzo, E., & Tsygankov, S. S. 2015, *A&ARv*, **23**, 2
- Wang, Y. M. 1996, *ApJL*, **465**, L111
- Wang, Z., Chakrabarty, D., & Muno, M. 2007, *ATel*, **1014**, 1
- Warwick, R. S., Marshall, N., Fraser, G. W., et al. 1981, *MNRAS*, **197**, 865
- Wenger, M., Ochsenein, F., Egret, D., et al. 2000, *A&AS*, **143**, 9
- White, N. E., Mason, K. O., Huckle, H. E., Charles, P. A., & Sanford, P. W. 1976, *ApJL*, **209**, L119
- White, N. E., & Pravdo, S. H. 1979, *ApJL*, **233**, L121
- White, N. E., Swank, J. H., & Holt, S. S. 1983, *ApJ*, **270**, 711
- Wilson, C. A., Finger, M. H., & Camero-Arranz, A. 2008, *ApJ*, **678**, 1263
- Wilson, C. A., Finger, M. H., Coe, M. J., Laycock, S., & Fabregat, J. 2002, *ApJ*, **570**, 287
- Wilson, C. A., Finger, M. H., Coe, M. J., & Negueruela, I. 2003, *ApJ*, **584**, 996
- Wilson, C. A., Finger, M. H., Harmon, B. A., et al. 1997, *ApJ*, **479**, 388
- Wilson, C. A., Finger, M. H., Harmon, B. A., Chakrabarty, D., & Strohmayer, T. 1998, *ApJ*, **499**, 820
- Wilson, C. A., Finger, M. H., & Scott, D. M. 1999, *ApJ*, **511**, 367
- Wilson, C. A., Strohmayer, T., & Chakrabarty, D. 1996, *IAUC*, **6514**, 2
- Wilson, C. A., Weisskopf, M. C., Finger, M. H., et al. 2005, *ApJ*, **622**, 1024
- Wilson, R. B., Fishman, G. J., Finger, M. H., et al. 1993, in *AIP Conf. Ser.* **280**, ed. M. Friedlander, N. Gehrels, & D. J. Macomb, 291
- Wilson, R. B., Zhang, S. N., Scott, M., et al. 1995, *IAUC*, **6207**, 1
- Wilson-Hodge, C. A. 1999, PhD thesis, Univ. Alabama in Huntsville
- Wilson-Hodge, C. A., Case, G. L., Cherry, M. L., et al. 2012, *ApJS*, **201**, 33
- Wilson-Hodge, C. A., Malacaria, C., Jenke, P. A., et al. 2018, *ApJ*, **863**, 9
- Woods, P. M., Kouveliotou, C., Finger, M. H., et al. 2007, *ApJ*, **654**, 470
- Yan, J., Zhang, P., Liu, W., & Liu, Q. 2016, *AJ*, **151**, 104
- Yan, J., Zurita Heras, J. A., Chaty, S., Li, H., & Liu, Q. 2012, *ApJ*, **753**, 73
- Yungelson, L. R., Kuranov, A. G., & Postnov, K. A. 2019, *MNRAS*, **485**, 851
- Zanni, C., & Ferreira, J. 2013, *A&A*, **550**, A99
- Zhang, S. N., Harmon, B. A., Paciesas, W. S., et al. 1996, *A&AS*, **120**, 227